The Astrophysical Journal, 795:86 (17pp), 2014 November 1 doi:10.1088/0004-637X/795/1/86

ON THE DIVERSITY OF MAGNETIC INTERACTIONS IN CLOSE-IN STAR–PLANET SYSTEMS

A. Strugarek[1,2], A. S. Brun[2], S. P. Matt[3], and V. Réville[2]
[1] Département de physique, Université de Montréal, C.P. 6128 Succ. Centre-Ville, Montréal, QC H3C-3J7, Canada; strugarek@astro.umontreal.ca
[2] Laboratoire AIM Paris-Saclay, CEA/Irfu Université Paris-Diderot CNRS/INSU, F-91191 Gif-sur-Yvette, France
[3] Astrophysics group, School of Physics, University of Exeter, Stocker Road, Exeter EX4 4QL, UK
Received 2014 July 31; accepted 2014 September 17; published 2014 October 15

ABSTRACT

Magnetic interactions between close-in planets and their host star can play an important role in the secular orbital evolution of the planets, as well as the rotational evolution of their host. As long as the planet orbits inside the Alfvén surface of the stellar wind, the magnetic interaction between the star and the planet can modify the wind properties and also lead to direct angular momentum transfers between the two. We model these star–planet interactions using compressible magnetohydrodynamic (MHD) simulations, and quantify the angular momentum transfers between the star, the planet, and the stellar wind. We study the cases of magnetized and non-magnetized planets and vary the orbital radius inside the Alfvén surface of the stellar wind. Based on a grid of numerical simulations, we propose general scaling laws for the modification of the stellar wind torque, for the torque between the star and the planet, and for the planet migration associated with the star–planet magnetic interactions. We show that when the coronal magnetic field is large enough and the star is rotating sufficiently slowly, the effect of the magnetic star–planet interaction is comparable to tidal effects and can lead to a rapid orbital decay.

Key words: magnetohydrodynamics (MHD) – planets and satellites: dynamical evolution and stability – planet–star interactions – stars: winds, outflows

Online-only material: color figures

1. INTRODUCTION

More than a thousand planets have now been discovered orbiting distant stars. These planets span several orders of magnitudes in mass, radius, and semi-major axis, and 187 of them to date orbit very close ($r_{\rm orb} < 10\,r_\star$) to their host.[4] Due to their proximity they are interacting with their star in very different physical conditions in terms of interplanetary plasma density, pressure, wind velocity, and magnetic field strength, compared to any other planet in our solar system. Star–planet interactions (SPIs) can originate from tidal forces, magnetic fields, winds, and radiative processes (see Cuntz et al. 2000). They have local and global consequences on the system over a large range of timescales.

SPIs may cause enhanced chromospheric and coronal activity. For instance, evidence of chromospheric hotspots related to an orbiting planet have been observed in several systems (Shkolnik et al. 2005) and were theoretically modeled by Lanza (2008, 2012). For massive and sufficiently close planets, it was suggested that SPIs could lead to an overall increase of the stellar magnetic activity (e.g., traced by an increase in the X-ray and UV emissions from the star; see Kashyap et al. 2008; Shkolnik 2013) due to tidal (Cuntz et al. 2000) or magnetized (Cohen et al. 2011) interactions. In addition, SPIs were also proposed to be at the origin of super-flares (Rubenstein & Schaefer 2000), although the lack of correlations between super-flaring stars and hot-Jupiter hosts observed with *Kepler* (Shibayama et al. 2013) suggests other triggering mechanisms (see Shibata et al. 2013). Magnetic dynamos operate in the interior of stars and planets (for recent reviews, see Stevenson 2003; Charbonneau 2010; Jones 2011; Brun et al. 2013). It was recently suggested that even the dynamo operational mode itself may be influenced by the star–planet (tidal) interactions (Abreu et al. 2012; Charbonneau 2013), leading to potentially observable perturbations of, e.g., the spot cycle of the Sun.

On the planetary side, Zarka (2007) proposed that the magnetized SPIs (SPMIs) could lead to enhanced radio emissions in the planetary magnetosphere. Jardine & Collier Cameron (2008) characterized such emissions and showed that they mainly depend on the density and magnetic field profiles in the stellar wind (e.g., see Vidotto et al. 2012, for a detailed theoretical modeling of radio emissions in the τ Boo system). Enhanced evaporation of the planetary atmosphere, due to stellar coronal activity, has also been reported by Lecavelier des Etangs et al. (2010). Although the various emission enhancements have not been systematically observed in close-in planet systems (Donati et al. 2008; Fares et al. 2010), Scharf (2010) showed that the observed positive correlation between the X-ray luminosity of the system and the mass of the orbiting planet could be used as a probe to measure the planetary magnetic field. Hence, the various emission enhancements that may originate from SPIs could be used, at least in principle, to estimate some physical properties of exoplanets. The temporal variability, as well as the physical mechanisms at the origin of those emissions, are still today an active subject of research (Shkolnik et al. 2008; Miller et al. 2012).

SPIs also have a major influence on the global properties of star–planet systems. For instance, understanding the stellar radiation and the stellar wind local properties is key to determine how a planet interacts with its environment (see, e.g., Lammer et al. 2009), and ultimately to determine the zone of habitability around stars (Selsis et al. 2007). Tidal interactions are well known to lead to the spin-orbital synchronization (e.g., through the so-called tidal-locking mechanism) of close-in planets. They also have more subtle effects in star–planet systems (for a review, see Mathis et al. 2013) and can for instance affect the orbital evolution of the planet (Bolmont et al. 2012; Auclair-Desrotour et al. 2014; Zhang & Penev 2014) or even the stellar rotational

[4] http://exoplanet.eu/

evolution (Barker & Ogilvie 2011; Poppenhaeger & Wolk 2014). In addition, magnetic interactions result in a torque applying to the orbiting planet, which also influences its migration (Laine et al. 2008; Lovelace et al. 2008; Vidotto et al. 2010; Lanza 2010; Laine & Lin 2011). If the planet orbits inside the Alfvén surface of the stellar wind (defined as the surface where the wind speed equals the local Alfvén speed), torques apply to the star as well and lead to a modification of its rotational history (Cohen et al. 2010). In some extreme cases, the SPIs can lead to the expansion of the planetary atmosphere beyond its Roche lobe, resulting in a constant outflow from the planet to the star which will also affect the orbital properties, as well as the stellar rotational history (Lai et al. 2010).

The development of a model describing the numerous SPIs, for the different types of stars and planets, is a formidable challenge but is extremely valuable for our understanding of the creation and evolution of planetary systems, and for the characterization of the observed exoplanetary systems. An ultimate goal is to develop a theoretical framework, based on numerical simulations, in which all the SPI effects could be taken into account, self-consistently. We focus the present work on the less-studied magnetized interaction, and more specifically on aspects of long-term impacts a close-in planet can exert on its host star. This simplified model uses a 2.5D (axisymmetric) geometry for simplicity, and will provide the basis for future and more detailed models.

Various definitions of the term *close-in* planet have been used in the literature. Here, we define a close-in planet as a planet that is able to influence its host star through magnetic interactions. Said differently, we consider close-in planets to be orbiting inside the Alfvén radius of the stellar wind. Alfvén waves excited by the presence of an orbiting planet can then travel from the planet vicinity to the stellar surface, where they are able to modify the plasma properties. Most studies of the SPMIs so far have been focused on their effects on the planetary dynamics (either fast magnetospheric evolution or slow planet migration, see Cohen et al. 2014, for a recent example), rather than describing the important feedback such a planet can exert on its host star on a secular timescale (see Cohen et al. 2010, for a notable first study of such long-term effect). The long term impact of SPMI can be two-fold: the magnetic torque leads to a direct transfer of angular momentum between the two bodies, and the magnetic interaction can modify the wind driving in the stellar corona. Modeling the latter requires taking into account coronal feedbacks in the wind driving mechanism.

We build our study on stellar wind models pioneered by Washimi & Shibata (1993) and further developed by, e.g., Keppens & Goedbloed (1999), Matt & Balick (2004), Matt & Pudritz (2008), Matt et al. (2012), Strugarek et al. (2014), Réville et al. (2014). These models possess good conservation properties and are designed to adapt to external perturbations (Strugarek et al. 2014). We develop in this work a numerical model for thermally driven winds (Section 2), in which close-in planets are introduced at various orbital radii (Section 3). We investigate the cases of magnetized—with different topologies—and unmagnetized planets, to systematically characterize the magnetized angular momentum transfers occurring in star–planet systems, along with the modification of the stellar wind induced by the SPMI (Section 4). We propose scaling laws for the effect of SPMIs in Section 5 and summarize our main findings in Section 6.

2. STELLAR WIND MODEL

We compute solutions for steady-state stellar winds, using the finite volume magnetohydrodynamic (MHD) code PLUTO (Mignone et al. 2007). We detail in Section 2.1 our simulation method and in Section 2.2 the fiducial stellar wind model selected to study the SMPIs.

2.1. Simulation Method

The PLUTO code solves the following set of ideal MHD equations:

$$\partial_t \rho + \boldsymbol{\nabla} \cdot (\rho \mathbf{v}) = 0 \tag{1}$$

$$\partial_t \mathbf{v} + \mathbf{v} \cdot \boldsymbol{\nabla} \mathbf{v} + \frac{1}{\rho} \boldsymbol{\nabla} P + \frac{1}{\rho} \mathbf{B} \times \boldsymbol{\nabla} \times \mathbf{B} = \mathbf{g}\,, \tag{2}$$

$$\partial_t P + \mathbf{v} \cdot \boldsymbol{\nabla} P + \rho c_s^2 \boldsymbol{\nabla} \cdot \mathbf{v} = 0\,, \tag{3}$$

$$\partial_t \mathbf{B} - \boldsymbol{\nabla} \times (\mathbf{v} \times \mathbf{B}) = 0\,, \tag{4}$$

where ρ is the plasma density, $\mathbf{v}$ its velocity, P the gas pressure, $\mathbf{B}$ the magnetic field, $\mathbf{g}$ the gravitational acceleration (which is time-independent), and $c_s = \sqrt{\gamma\, P/\rho}$ the sound speed (γ is the adiabatic exponent, taken to be the equal to the ratio of specific heats). We use an ideal gas equation of state

$$\rho \varepsilon = P/(\gamma - 1)\,, \tag{5}$$

where ε is the internal energy per mass.

We use the following numerical method implemented in the PLUTO code. First, a minmod limiter is used on all the variables, combined to a *hll* (Harten, Lax, Van Leer) solver to compute the intercell fluxes. A second order Runge–Kutta scheme is used for the time evolution. The solenoidality of the magnetic field ($\boldsymbol{\nabla} \cdot \mathbf{B} = 0$) is ensured with a *constrained transport* method (see Evans & Hawley 1988; Gardiner & Stone 2005). We use a 2.5D geometry, centered on the rotating star, meaning that we solve the equations for fully three-dimensional (3D) vector components of the velocity and magnetic fields, but assume an axisymmetric geometry.

Following the work of Matt et al. (2012), we initialize our simulations with a spherically symmetric, hydrodynamic Parker wind solution (Parker 1958), to which we add a dipolar magnetic field with a magnetic moment $\mu_\star$. We developed special boundary conditions at the base of the wind (after Matt & Balick 2004) that ensure good conservation properties (Lovelace et al. 1986; Keppens & Goedbloed 2000; Zanni & Ferreira 2009) along the magnetic field lines. They consist of three circular layers representing the lower corona in which the Parker wind pressure gradient, the rotation rate of the star, and its magnetic field are successively imposed. They are designed as follows.

1. *Upper layer.* The density and pressure are fixed to the one-dimensional (1D) Parker wind solution. The poloidal (ϖ, z) velocity field is forced to be parallel to the poloidal magnetic field, while its magnitude can evolve freely. The azimuthal velocity and the magnetic field are left free to evolve.
2. *Middle layer.* The density and pressure are fixed to the 1D Parker wind solution. The poloidal velocity is set to zero, and the azimuthal velocity is fixed to the stellar rotation. The magnetic field is left free to evolve.

3. *Lower layer.* The density and pressure are fixed to the 1D Parker wind solution. The poloidal velocity is set to zero and the azimuthal velocity is fixed to the stellar rotation. The poloidal magnetic field is fixed to the dipolar stellar field. In the open field line regions B_φ is set to minimize the poloidal currents. In the closed field line regions B_φ is set to zero. The open and closed field line regions are distinguished based on a local criterion involving the azimuthal Alfvén speed, which allows us to dynamically identify the various regions as the wind evolves.

We also observed that adding one more layer above the stellar surface, where the poloidal velocity field is forced to be parallel to the poloidal magnetic field, improves the conservation properties of the model. All the models presented in this work use this additional layer.

When a planet is included in the model, the density and pressure are held fixed to specified values in the planetary interior. The poloidal velocity is fixed to zero and the azimuthal velocity to the Keplerian velocity in the whole planetary interior. In the unipolar cases (see Section 3.2), the magnetic field is free to evolve inside the planet, and in the dipolar cases (see Section 3.3), it is held fixed to the planetary dipole.

Our boundary conditions allow the wind driving to automatically adapt to external perturbations originating from the star–planet magnetic connection. We impose outflow conditions on the outer boundaries (zero-gradient imposed on all quantities), and axisymmetry at the rotation axis. We refer the reader to Strugarek et al. (2014) for a more complete discussion on boundary conditions.

The stellar radius is uniformly discretized over 64 grid points in the radial direction and is discretized over two uniform domains in the vertical direction to ensure a higher resolution on the equatorial plane where the planet lies. The circular planet is discretized with a square of 64^2 grid points (we adapt the grid for each planetary orbital radius considered in this work). The rest of the domain is discretized with stretched grids, giving a typical overall resolution of 400 points in the radial direction and 384 in the vertical direction. The grid for models with an orbital radius of $3\,r_\star$ is shown in Figure 1, with two insets zooming on the stellar and planetary boundaries.

In the planet-free case, a steady-state stellar wind is typically obtained after a few sound crossing times, when the accelerating wind and rotating magnetic field are dynamically balanced. The solution for the wind depends on three velocity ratios defined at the surface of the star, and on the ratio of specific heats γ. The three characteristic velocities are the sound speed c_s, the Alfvén speed $v_A = B_\star/\sqrt{4\pi\rho_\star}$ (where $B_\star = \mu_\star/r_\star^3$ is the magnetic field strength at the stellar equator) and the rotation speed $v_{\rm rot}$ (in this work, the star is considered to rotate as a solid body). Their ratios to the escape velocity $v_{\rm esc} = \sqrt{2GM_\star/r_\star}$ at the stellar surface then define a unique stellar wind solution. The global properties of the wind can be characterized by its mass loss rate $\dot{M}_\star$ and its angular momentum loss rate (AML) $\dot{J}_\star$, which are computed a posteriori and defined by (e.g., Matt & Balick 2004)

$$\dot{M}_\star = \oint \rho \mathbf{v} \cdot d\mathbf{A}\,, \tag{6}$$

$$\dot{J}_\star = \oint \varpi \left(v_\phi - B_\phi \frac{\mathbf{v}_p \cdot \mathbf{B}_p}{\rho |\mathbf{v}_p|^2}\right) \rho \mathbf{v} \cdot d\mathbf{A}\,, \tag{7}$$

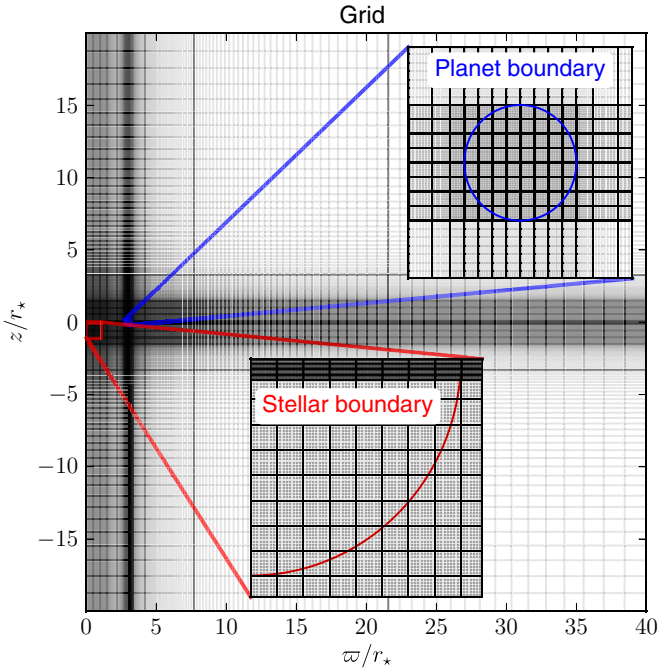

Figure 1. Grid of the $r_{\rm orb} = 3\,r_\star$ cases. The grid is highlighted every 32 points. The two insets are zooms on the southern hemisphere of the star and on the planet location. The boundaries of the star and the planet are labeled in red and blue. In those insets the grid is highlighted every eight points.

(A color version of this figure is available in the online journal.)

where (ϖ, ϕ, z) is the cylindrical coordinate system, the subscript p denotes the poloidal (ϖ, z) component of a vector, and $\oint \mathbf{x} \cdot d\mathbf{A}$ stands for the integral of $\mathbf{x}$ on a spherical surface enclosing the star. Because mass and momentum are conserved, a steady-state requires the spherical integrals (6) and (7) to be constant in between sources and sinks (here, the star and the planet) in the domain. Hence, the integrals can be equivalently evaluated on any spherical surface when a statistical steady-state is reached in the simulation.

2.2. Fiducial Stellar Wind

Depending on the choice of parameters, the simulated stellar winds possess a variable size dead-zone (i.e., the zone where the magnetic pressure is high enough to confine the plasma and suppress the wind driving; see, e.g., Mestel 1968; Keppens & Goedbloed 1999; Matt & Pudritz 2008). The relative position of the Alfvén surfaces and the dead-zone radius can also vary significantly. The three Alfvén surfaces label the position in the stellar wind at which the three following magnetic Mach number are equal to unity (Keppens & Goedbloed 1999),

$$(M_A)^2 = \frac{v_\varpi^2 + v_z^2 + v_\phi^2}{A_\varpi^2 + A_z^2 + A_\phi^2}\,, \tag{8}$$

$$(M_s)^2 = \frac{2\left(v_\varpi^2 + v_z^2\right)}{c_s^2 + A_p^2 + A_\phi^2 - \sqrt{\left[c_s^2 + A_p^2 + A_\phi^2\right]^2 - 4c_s^2 A_p^2}}\,, \tag{9}$$

$$(M_f)^2 = \frac{2\left(v_\varpi^2 + v_z^2\right)}{c_s^2 + A_p^2 + A_\phi^2 + \sqrt{\left[c_s^2 + A_p^2 + A_\phi^2\right]^2 - 4c_s^2 A_p^2}}\,, \tag{10}$$

Table 1
Stellar Wind Parameters and Characteristics

Parameter	Value
γ	1.05
$c_s/v_{\rm esc}$	0.2599
$v_A/v_{\rm esc}$	0.3183
$v_{\rm rot}/v_{\rm esc}$	0.00303
Characteristics	**Value**
ρ_0 (g cm^{-3})	1.3e-16–1.3e-11
$B_\star$ (G)	0.78–246
$\dot{M}_\star$ ($M_\odot$ yr^{-1})	2e-14–2e-9
$\dot{J}_\star$ ($M_\odot$ $R_\odot^2$ yr^{-2})	4e-11–4e-6

where $\mathbf{A} = \mathbf{B}/\sqrt{4\pi\rho}$. We use r_a and r_f to denote the positions of the Alfvén surface ($M_A = 1$) and fast Alfvén surface ($M_f = 1$) on the equatorial plane. We build a simulation with parameters listed in Table 1, following on the preliminary study of Strugarek et al. (2012). Because we work with dimensionless quantities, a single wind simulation may represent different physical winds depending on the normalization. For a given simulation, the density normalization ρ_0 directly sets the physical amplitude of the stellar magnetic field. The physical mass loss rate is then determined by the radius and mass of the star, which we consider here to be solar. We give in Table 1 their physical values, as well as the mass and angular momentum loss rates of the modeled stellar wind for two possible density normalizations. The two density normalizations were chosen to represent a solar-like mass loss rate in the first case, and in the second case a very large mass loss rate that is thought to be representative of young Suns or T Tauri stars. It corresponds to a variation of five orders of magnitude of ρ_0. The magnetic field of 246 G in the second case is quite large, it is likely to represent an upper limit case for the potential effects of the SPMIs. Finally we define the torque applied by the (fiducial) wind to the star, $\tau_w = -\dot{J}_\star$, which will be used as a normalization to the magnetic torques in the remainder of this work. In all cases, the modeled stellar wind reaches 450 km s^{-1} near 1 AU, which is representative of the "slow" component of the solar wind.

The resulting stellar wind is displayed in Figure 2. The initial magnetic dipole has opened up under the influence of the accelerating wind, leaving a dead-zone near the equator where the field lines remain closed. The three Alfvén surfaces are delimited by the white lines. In this case, the Alfvén surface coincides with the fast Alfvén surface at the poles and with the slow Alfvén surface ($M_s = 1$) at the equator (Keppens & Goedbloed 1999). Note that the surface where the Mach number is one ($\mathbf{v}_p = c_s$, black line in Figure 2) coincides with those surfaces in an exactly opposite way. We obtain the position of the Alfvén surface on the equatorial plane $r_a \sim 3.5\,r_\star$ and the position of the fast Alfvén surface averaged on a thin disk centered on the equator $r_f \sim 7\,r_\star$.

We focus in this work on the magnetic feedback close-in planets can exert on their host stars. Such planets necessarily orbit inside the fast-Alfvén surface to enable Alfvén waves to travel from the planet to the stellar surface. Indeed, a planet orbiting outside the Alfvén surfaces can be influenced by the magnetized stellar wind (e.g., Vidotto et al. 2014), by stellar radiation and by tides, but it cannot back-react magnetically on its host star. The SPMI is driven by the differential motion between the orbiting planet and the rotating wind. The positions of the Alfvén surfaces and the rotation rate of the wind can be a priori estimated from our knowledge of thermally driven stellar

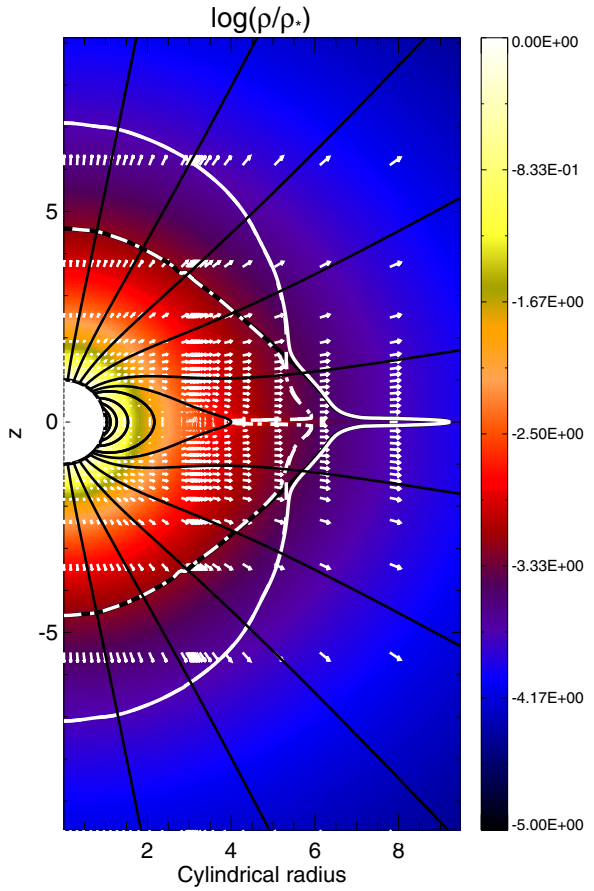

Figure 2. Fiducial stellar wind. Axes are given in units of stellar radius. The color map represents the logarithm of the wind density, normalized to the stellar surface density. White arrows show the local poloidal wind velocity. The magnetic field lines are displayed in solid black lines. Four characteristic surfaces are shown: the fast (three dot–dashed white line), slow (dot–dashed white line), and classic (dashed white line) Alfvén surfaces (see Equations (8)–(10)), and the surface at which the local Mach number is equal to one (thick black line). The stellar surface is indicated by a black half circle.
(A color version of this figure is available in the online journal.)

wind. On the equatorial plane, for a dipolar-type thermally driven stellar wind, a dead-zone co-rotating with the star extends roughly from the stellar surface to the Alfvén surface. The fast Alfvén surface generally extends further away from the star, and the rotation profile of the region in between roughly falls proportionally to the inverse of the distance to the star. The approximate equatorial position of the Alfvén surface can be semi-analytically derived with the same methodology used by Matt et al. (2012) and Réville et al. (2014). Matt et al. (2012) showed that a stellar wind could be unambiguously characterized, either by its mass- and angular momentum loss rates, or, equivalently, by the stellar equatorial rotation speed f and a parameter Υ, representing a dimensionless mass loss rate (similar to the magnetic confinement parameter of ud Doula & Owocki 2002) and defined by

$$f = \Omega_\star r_\star^{3/2} (GM_\star)^{-1/2} = \sqrt{2}\,\frac{v_{\rm rot}}{v_{\rm esc}}\,, \tag{11}$$

$$\Upsilon = B_\star^2 r_\star^2 \left(\dot{M}_\star v_{\rm esc}\right)^{-1} = \frac{4\pi\rho_\star r_\star^2 v_{\rm esc}}{\dot{M}_\star}\left(\frac{v_A}{v_{\rm esc}}\right)^2\,, \tag{12}$$

where $\Omega_\star$ is the stellar angular rotation rate. Using the grid of stellar wind models described in Réville et al. (2014), we fit the

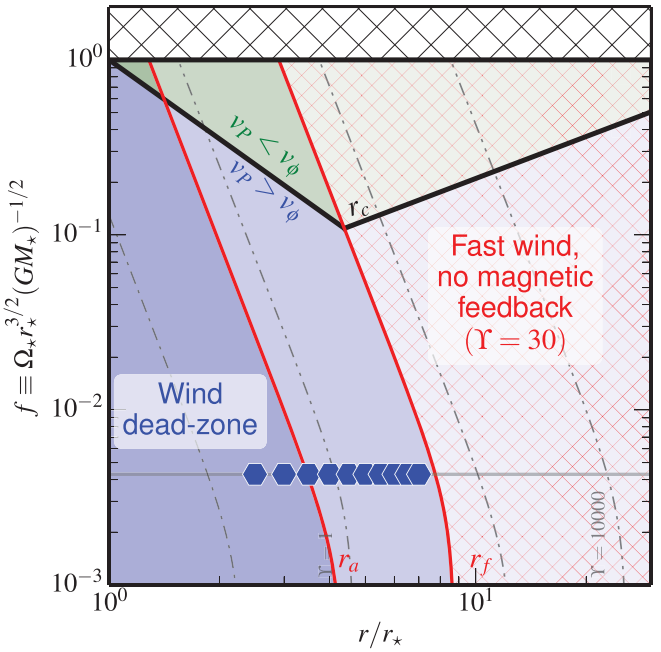

Figure 3. Wind characteristics as a function of rotation rate (vertical axis) and distance to the star (horizontal axis). The position of the Alfvén (r_a) and fast Alfvén (r_f) surfaces are shown in red for $\Upsilon = 30$ and dashed–dotted lines for $\Upsilon = 1$ and 10^4. The radius r_c where the Keplerian velocity is equal to the azimuthal velocity of the wind is labeled by the inclined black lines. The Alfvén surfaces delimit the dead-zone and the fast wind regions. The top hatched region corresponds to the unphysical case of stars with surface velocities higher than the Keplerian velocity. The orbital radii considered in this paper are given by the blue hexagons overlaid on the rotation rate of the fiducial star (horizontal grey line).

(A color version of this figure is available in the online journal.)

Alfvén equatorial radii[5] to the wind parameters (Υ, f) with

$$\frac{r_{a,f}}{r_\star} = K_1^{a,f}\left(\frac{\Upsilon}{\sqrt{1+(f/K_2)^2}}\right)^{m^{a,f}}. \quad (13)$$

The fitted parameters K_1, K_2, and m are given in Table 2.

The position of the Alfvén equatorial radii is illustrated in Figure 3. The Alfvén surface position is shown as a function of the fraction of break-up spin rate f (vertical axis) and magnetic confinement parameter Υ (pairs of oblique curves). The particular case of $\Upsilon = 30$ (red curves), which corresponds to the fiducial stellar wind considered in this work, is highlighted.

The orbital velocity of the planet is Keplerian. For the sake of simplicity, we assume a circular orbit for the planet. The orbital velocity only depends on the stellar mass and the orbital distance and is given by $v_P = \sqrt{GM_\star/r_{\rm orb}}$ (under the approximation $M_p/M_\star \ll 1$). In Figure 3 the black oblique lines represent the radii r_c at which the Keplerian velocity is equal to the rotational velocity of the wind. It separates two interaction regions where the orbital velocity of the planet is higher (blue areas) and lower (green areas) than the azimuthal velocity of the rotating wind. Any planet orbiting outside the r_f curve (red hatched area) cannot magnetically influence the star. A planet orbiting inside r_a generally rotates much faster than the wind itself (blue areas), although in the case of rapidly rotating stars the opposite situation may happen (green areas).

The SPMI is initially driven by the difference in azimuthal velocity between the orbiting planet and the rotating wind. It is important to realize that the orbital velocity of the planet v_P is a function of $r_{\rm orb}^{-1/2}$, whereas the orbital angular momentum of the planet is a function $r_{\rm orb}^{1/2}$. If $v_P > v_\phi$, a positive transfer of angular momentum from the planet to the star develops and leads to a decrease of the orbital angular momentum. This decrease necessarily leads to an increase of the planetary orbital velocity (and a decrease of the orbital radius; see also Lovelace et al. 2008; Laine & Lin 2011) as well as an increase in the stellar rotation rate that should be accompanied by an increase of the stellar wind rotation.

Depending on the position of the planet in the wind, two situations can occur. Inside the dead-zone, the planet's orbital frequency usually increases faster than the stellar rotation frequency (this is true for $r_P/r_\star \lesssim 0.5(M_\star/M_P)^{1/2}$). As a consequence, the differential motion between the planet and the wind increases and strengthens the SPMI. The planet migration associated with the SPMI is therefore *unstable*. A planet orbiting at the exact same rate as the stellar wind should not transfer angular momentum magnetically to the star, but the instability is such that any perturbation would tend to grow and to make the planet migrate. If the planet is inside the co-rotation radius (blue areas), the SPMI leads to an orbital decay of the planet until it reaches its Roche radius or simply merges with its host. If the planet lies outside the co-rotation radius (green areas), the SPMI leads to an outward migration of the planet.

Outside the Alfvén radius (red hatched zone), the azimuthal velocity of the wind falls off with cylindrical radius, and if the star rotates fast enough, a stable point exists where the planet is in co-rotation with the wind (black oblique line in the hatched zone). Of course, the stellar evolution, the tidal interactions between the planet and its host, other rotating planets, or even a disk should also be considered to determine the final migration path of the planet (see Bolmont et al. 2012; Zhang & Penev 2014, for recent efforts to model the evolution of such systems including the effects of tides).

The positions of the Alfvén surfaces are also plotted for much weaker and stronger magnetic fields ($\Upsilon \in \{1, 10^4\}$) in grey dash–dotted and dash–double dotted lines, for reference. The interaction region where a planet is able to provide magnetic feedback to its host grows with decreasing stellar rotation rate and decreasing mass loss rate/increasing $B_\star$ (increasing Υ). This is a direct consequence of the shrinking/expansion of the Alfvén surfaces in the equatorial plane (Equation (13)). It must be stated here that in reality, the magnetic interaction regions are likely to be even more complex. We have assumed here a dipolar topology for the stellar wind. For other magnetic topologies the Alfvén surface on the stellar equator can be pushed closer the stellar surface (Réville et al. 2014). In the more realistic case of non-axisymmetric and/or cyclic magnetic fields, the radial location of the Alfvén surface on the equator in the frame rotating with the orbiting planet is time dependent (see also Pinto et al. 2011), which leads to a significant modulation of the interaction regions.

Table 2
Fit Parameters for the Position of Alfvén Surfaces on the Equatorial Plane

	K_1	K_2	m
r_a	2.3027	0.0014	0.1842
r_f	4.8412	0.0027	0.1858

[5] Note that this is an *equatorial* value, and not the torque-determined globally averaged value used in Matt et al. (2012) and Réville et al. (2014).

Finally, the magnetic interaction efficiency between a star and planet also strongly depends on the planet characteristics, which will be explored in the following sections. In order to restrain the parameter space to study, we will focus here on one type of stellar wind labeled by the horizontal grey line in Figure 3 and vary the planet parameters (blue hexagons). As can be seen in Figure 3, the results can be translated accordingly for different stellar rotation rates and different mass loss rates.

3. PLANET MODELS

The axisymmetric geometry we consider is a first step toward a more realistic modeling. It does not allow us to fully describe the intrinsically 3D star–planet system: the planet is effectively represented by an axisymmetric torus of large radius $r_{\rm orb}$ and small radius r_P. Nevertheless, Cohen et al. (2010) showed that even in the 3D global geometry, a planet affects the stellar wind globally (i.e., at all longitudes). In addition, our reduced 2.5D geometry captures the basic physical ingredients of SPMIs, as will be made clear in the two following sections. As a first step, we chose the axisymmetric 2.5D approach, in order to explore a large parameter space, while still adequately modeling the physical processes impacting the star. These impacts are likely to be overestimated in this study compared to a more realistic 3D case, which we leave for future work.

3.1. Simulation Method and Planet Characteristics

We initialize a circular (in the (ϖ, z) plane) planet at an orbital radius $r_{\rm orb}$ at the same time as the initialization of the stellar wind. The planet's gravitational potential is added to the stellar potential in the whole domain. The planet itself is modeled as a boundary region in which the pressure, density, velocity and magnetic field have to be prescribed. In all cases, we hold both the orbital radius and the orbital velocity of the planet constant (see Strugarek et al. 2014, for more details). This is justified a posteriori by the fact that the torques that develop in the system will make the planet migrate over much longer timescales than the overall simulated temporal evolution. Given its proximity to its host star, the planet's rotation period is considered to be synchronized with the orbital period due to tidal locking. The system reaches a steady-state on a timescale of a few sound crossing times. We checked that doubling the resolution does not change our results by more than 3% in the magnetized-planet case (see Section 3.3). In this case the planetary field creates a shield around the planet that is barely affected by changes in the resolution. However, the non-magnetized planet cases (see Section 3.2) show a stronger dependency upon the grid resolution of our model: doubling the overall resolution leads to variations of 30% of the torque applied by the planet to the star. This stronger resolution dependence is expected since, in the unipolar case, the resolution inside the planet determines the level of numerical dissipation in the planetary interior, which ultimately counterbalances the induction, once a steady-state is reached. Even though the numerical value of the torques can be affected by the grid resolution, the trends we derive in Sections 4 and 5 remain robust.

We choose typical "hot-Jupiter" characteristics for our modeled planet. We set its radius to $r_P = 0.1\,r_\star$ and its mass to $M_P = 0.01\ M_\star$. Considering spherical bodies and a circular orbit for the planet, we can calculate the Roche limit $d_{s,fl} = \alpha_{s,fl} r_P\,(M_\star/M_P)^{1/3}$, with the coefficients $\alpha_s = 1.26$ in the solid case and $\alpha_{fl} = 2.44$ in the fluid case. The parameters we chose for our study lead to $d_s = 0.59\,r_\star$ and $d_{fl} = 1.13\,r_\star$ in the solid and fluid cases. Hence, all the orbital radii considered here lie well outside the Roche limit of the star–planet system. Such a choice of parameters corresponds closely to the observed Corot-27 b (Parviainen et al. 2014) or WASP-18 b (Hellier et al. 2009; Southworth et al. 2009) planets.

Table 3
Parameters and Results of the SPMI Cases

Case	$r_{\rm orb}/r_\star$	θ_0	B_P/B_w	$r_{\rm m}/r_P$	$\tau_w^\star/\tau_w$	$\tau_P^\star/\tau_w$	τ^P/τ_w
U2.5	2.5	...	...	...	0.85	−3.50	2.96
U3	3.0	...	...	...	0.71	−1.55	1.33
U3.5	3.5	...	...	...	0.70	−0.95	0.86
U4	4.0	...	...	...	0.77	−0.59	0.57
U4.5	4.5	...	...	...	0.83	−0.26	0.30
U5	5.0	...	...	...	0.86	−0.09	0.13
U5.5	5.5	...	...	...	0.94	−0.01	0.04
U6	6.0	...	...	...	0.99	<1%	<1%
U6.5	6.5	...	...	...	1.00	<1%	<1%
U7	7.0	...	...	...	1.00	<1%	<1%
D2a0	2.5	0	$7.5\ 10^0$	1.7	0.89	−1.14	1.36
D2r0	2.5	π	$7.5\ 10^0$	2.5	0.74	−2.59	5.26
D3a0	3.0	0	$3.4\ 10^1$	1.4	0.69	−0.40	0.40
D3a1	3.0	0	$3.4\ 10^2$	3.1	0.64	−0.43	0.44
D3a2	3.0	0	$8.4\ 10^2$	4.6	0.56	−0.46	0.48
D3ia0	3.0	$\pi/4$	$3.4\ 10^1$	1.6	0.84	−0.02	0.04
D3ia1[a]	3.0	$\pi/4$	$3.4\ 10^2$	3.3	0.65–0.75	−0.93–−0.02	0.02–1.01
D3ia2	3.0	$\pi/4$	$6.7\ 10^2$	4.4	0.65	−1.40	1.36
D3i0[a]	3.0	$\pi/2$	$3.4\ 10^1$	1.7	0.86–0.90	−0.17–−0.01	0.03–0.20
D3i1[a]	3.0	$\pi/2$	$6.7\ 10^1$	2.3	0.82–0.84	−0.87–−0.47	0.46–0.87
D3i2	3.0	$\pi/2$	$3.4\ 10^2$	3.5	0.67	−2.32	4.04
D3ir0	3.0	$3\pi/4$	$3.4\ 10^1$	1.9	0.79	−0.58	0.59
D3ir1	3.0	$3\pi/4$	$1.0\ 10^2$	2.7	0.83	−1.86	2.57
D3ir2	3.0	$3\pi/4$	$3.4\ 10^2$	4.5	0.77	−2.99	4.60
D3r0	3.0	π	$3.4\ 10^1$	1.8	0.73	−0.46	0.84
D3r1	3.0	π	$6.7\ 10^1$	3.3	0.75	−1.23	2.33
D3r2	3.0	π	$3.4\ 10^2$	6.2	0.77	−3.22	5.83
D4.5a0	4.5	0	$1.7\ 10^3$	3.8	0.87	−0.11	0.32
D4.5r0	4.5	π	$1.0\ 10^3$	5.0	0.72	−0.32	1.06
D6a0	6.0	0	$2.0\ 10^3$	4.8	0.99	<1%	0.21
D6a1	6.0	π	$6.1\ 10^2$	5.2	0.93	−0.01	0.33

Note. [a] Cases that oscillate between open and confined magnetic configurations.

Following the terminology proposed by Zarka (2007) (see also Kivelson et al. 2004) in the context of Jovian satellites, we consider both the cases of *unipolar* (weakly or non magnetized planet, hereafter labeled U) and *dipolar* (strongly magnetized planet with respect to the interplanetary medium, hereafter labeled D) interactions. Those two cases could represent hot Jupiter (Lanza 2009) or Super-Earth (Laine et al. 2008) close-in planets. We describe those two types of interactions in detail in Sections 3.2 and 3.3 respectively. A list of all the simulations described in this work can be found in Table 3.

3.2. Unipolar Interaction

The unipolar interaction refers to an interaction of a magnetized medium with a weakly (or non-) magnetized obstacle. In the context of SPMI, the magnetized medium is the stellar wind and the obstacle is the planet. This interaction was initially modeled in the context of the Io–Jupiter system by Goldreich & Lynden-Bell (1969). Several unipolar interaction cases need to be distinguished.

In the solar system, Venus provides an example of unipolar interaction between a planet and the wind of its host star. Although Venus possess no intrinsic magnetic field, it has

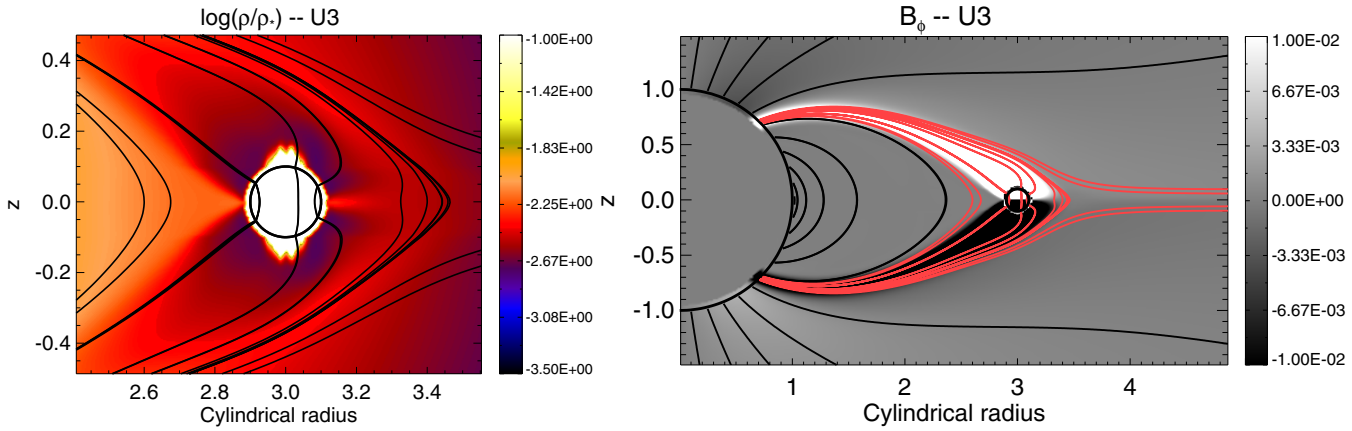

Figure 4. Unipolar interaction case U3. The planet is located at $r_{\rm orb} = 3\,r_\star$. The left panel represents the plasma density (in log scale) normalized to the stellar coronal base density. The planet surface is shown by a black circle. The solid black lines are magnetic field lines. The right panel shows the azimuthal component of the magnetic field (black and white map). The solid lines are the poloidal magnetic field lines, which are emphasized in red in the planet vicinity.

(A color version of this figure is available in the online journal.)

a neutral atmosphere that is efficiently screened from the surrounding solar wind by its ionosphere. More precisely, the very high ionospheric conductivity prevents the solar wind magnetic field from permeating into the atmosphere of Venus (Russell 1993). Such unipolar cases lead to the creation of an induced magnetosphere in the planet vicinity, which possess the same global structure—from the point of view of the wind—as the self-generated (via an internal dynamo; see Stevenson 2003) magnetospheres of planets like the Earth or Jupiter, although the induced magnetospheres owe their origin to a completely different process and are generally much less spatially extended (for a recent modeling of the magnetosphere of Venus and its interaction with the solar wind plasma, see Ma et al. 2013).

It must be noted, however, that a planetary ionosphere does not always provide an effective magnetic shield to the ambient stellar wind. The ionospheric barrier can indeed break if the stellar wind is sufficiently dense, sufficiently fast, or if the stellar ionizing influence (through either ion pick-up or high energy radiation) is sufficiently low (Russell 1993). Such conditions can be realized for close-in exoplanets that interact with a much more dense stellar wind than distant planets do. In this case, the wind magnetic field can permeate into the planetary interior. The interaction that develops in this case is the so-called generalized Alfvén wings scenario (Neubauer 1998). We consider here a simplified, ideal MHD formulation of the problem, in which the Alfvénic perturbations associated with the planet are either reflected and absorbed at the stellar boundary, or travel to the outer boundaries of the domain. Models taking into account a finite conductivity of the ambient plasma, where the waves can be reflected in between the two bodies, can be found in, e.g., Neubauer (1980) and Kivelson & Ridley (2008). In addition, because of the axisymmetric geometry we consider here, any reflected perturbation will always come back to the orbiting planet and the planet will behave as the so-called unipolar inductor (Goldreich & Lynden-Bell 1969). Then, two extreme cases may occur (Laine et al. 2008). If the planetary electric conductivity is very high compared to the stellar surface conductivity, magnetic field lines are frozen in the planet and dragged as the planet orbits (Laine & Lin 2011). Conversely, if it is very low, the wind magnetic field diffuses through the planet. For moderate conductivities, one would expect that both effects play a role in the SPMI. A slipping time can be defined by the time it takes a magnetic flux tube to slip through the planet. The slipping time depends on the relative orbital motion of the planet in the ambient rotating wind, and on the ratio of the electric conductivities between the planetary interior and the stellar surface. The reduced 2.5D axisymmetric geometry we chose for this first study allows us to model only the case where the planet drags the magnetic field as it orbits (similar to the Io–Jupiter case, with a closed current circuit between the planet and its host; see Strugarek et al. 2012).

A full treatment of the various unipolar cases would require the description of the ionization of the planetary atmosphere by the stellar wind and stellar UV radiation, which is beyond the scope of this study. This effect, combined with diffusive effects acting in the planet interior, is left for future work. Furthermore, the geometry in the induced magnetosphere case cannot be realistically modeled with a 2.5D axisymmetric setup; hence, we will focus our study on the unipolar case with no induced magnetosphere.

We let the magnetic field freely evolve inside the planet and fix all the other variables. The density profile inside the planet then determines the development of the SPMI. We tested various radial shapes of the density profile (from constant to Gaussian) under the constraint of a given planetary mass. We found that the density jump between the planet surface and the ambient wind is the important control parameter for the level of interaction the system is able to reach. The detailed shape of the density profile inside the planet only marginally affects the SPMI properties. We varied the density contrast between the planet and the ambient stellar wind from 10^5 to 10^{20}. The torques that develop in the unipolar cases (results shown in Section 4, see Figure 8) depend linearly on the logarithm of this density contrast. On one hand, the modification of the stellar wind torque increases only by 3% between density ratios from 10^5 to 10^{20} and can hence be neglected. On the other hand, the torque applied by the planet to the star increases (in absolute value) by 25% due to the amplification of the azimuthal magnetic field in the flux tube linking the star and the planet. We choose in the remainder of this paper to consider a density contrast of 10^{13}. Our results are robust to small (factor of two) variations of the density contrast, but larger variations have to be taken into account when using the torque scalings that will be derived in Section 4.

Figure 4 displays the solution we obtained for case U3 (see Table 3), with a planet located at $3\,r_\star$ (just inside the dead-zone of the stellar wind). We show the density (left panel) in the a steady-state solution. A very thin, higher-density boundary layer is created around the planet. It does not pollute the wind plasma and its size is robust with respect to both the grid resolution and the density contrast. On the right panel the azimuthal magnetic field is shown by the black and white color map. The magnetic field lines connecting the planet to the star (and nearby field lines) are highlighted in red. We observe that the magnetic flux-tube is strongly elongated in the azimuthal direction, due to fast orbital motion of the planet in the relatively slowly rotating wind. The pitch-angle $|B_\phi/B_p|$ in the flux tube reaches values of $\sim$3 on the dayside of the planet. On the nightside, it reaches occasionally larger values ($<$10) that lead to a fast outward opening and reconnection of the magnetic field lines. The small magnetic lobes observed on the left panel in each hemisphere on the nightside of the planet are residuals from those occasional reconnection events. These events are reminiscent from the well known twisting/slipping mechanism (see, e.g., Matt & Pudritz 2005, in the context of star–disk interaction) and are a trace of the finite amount of dissipation imposed by our grid. The time dependence introduced by these events in our simulations are observed to have a negligible influence on the global properties of the star–planet system.

The boundary condition on pressure then determines whether or not some plasma escapes away from the surface of the planet. Because we are interested primarily in angular momentum transfers between the star and the planet, we chose here to neglect atmospheric escape and design the planet boundary conditions such that no outflow from the planet is generated. The same care was taken for the dipolar interaction cases, which we describe in the next section.

3.3. Dipolar Interaction

We enforce a dipolar field at the planetary surface in dipolar cases. We adapted the magnetic dipole formula for our planet—which is shifted from the origin of the study frame—so that it still satisfies $\boldsymbol{\nabla}\cdot\mathbf{B}=0$. Such a dipolar field is given by

$$B_\varpi = \mu_P \cos(\theta_0)\frac{3z\varpi'}{(\varpi'^2+z^2)^{\frac{5}{2}}} + \mu_P \sin(\theta_0)\frac{2z^2-\varpi'^2}{(\varpi'^2+z^2)^{\frac{5}{2}}}, \quad (14)$$

$$B_z = \mu_P \cos(\theta_0)\frac{z^2\left(2-\frac{r_{\rm orb}}{\varpi}\right)-\varpi'^2\left(1+\frac{r_{\rm orb}}{\varpi}\right)}{(\varpi'^2+z^2)^{\frac{5}{2}}} + \mu_P \sin(\theta_0)\frac{-3\varpi' z+\frac{z}{\varpi}(\varpi'^2+z^2)}{(\varpi'^2+z^2)^{\frac{5}{2}}} \quad (15)$$

where $\varpi' = \varpi - r_{\rm orb}$, μ_P is the dipolar moment of the planetary magnetic field and θ_0 is the tilt angle of the planetary dipole with respect to the vertical axis. The interaction of the magnetosphere with the coronal wind establishes a steady-state planetary magnetosphere of finite size. In all cases, the velocity of the planet is set to be Keplerian, and the other velocity components are set to zero at the surface of the planet. We define each case by the ratio of the planetary field at its pole ($B_P = \mu_P/r_P^3$) to the local wind magnetic field B_w (see Table 3).

In Figure 5 we display three dipolar interaction cases, for a planet located at $r = 3\,r_\star$ (inside the dead-zone of the stellar wind), with different magnetospheric angles θ_0 (see Table 3 for the cases parameters). We observe that, in all three cases, the planet is able to retain a magnetosphere, whose finite size depends on B_P/B_w, θ_0, and on the position of the planet in the wind. We define the size of the planetary magnetosphere r_m by the extend of the last closed magnetic field line of the planet on the planetary magnetic equator, on the dayside. The magnetospheric sizes for all the dipolar cases are shown in Table 3.

In all cases, there is a direct magnetic link from the magnetic poles of the planet to the star. For the wind considered here and a planet located at $r_{\rm orb} = 3\,r_\star$, the foot-point of the magnetic link on the stellar surface is located near the open-closed field lines transition region. The SPMI develops the same qualitative behavior in the unipolar and dipolar cases: elongated field lines with a strong positive (resp. negative) azimuthal magnetic field in the north (resp. south) hemisphere connect the star to the planet. The qualitative resemblance of all the SPMI cases suggests that the shape of the magnetic interaction between the two bodies is primarily determined by the strong coronal stellar magnetic field.

We observe, nonetheless, significant differences in the three dipolar cases displayed in Figure 5. Some magnetic field lines originating from the poles of the planet open in the stellar wind in the anti-aligned ($\theta_0 = \pi$) case. It is now well established that the direction of the planetary magnetic field naturally leads to a "closed" or an "open" interaction case (Ip et al. 2004). The closed configuration (upper panels in Figure 5) efficiently confines most of the plasma inside the planetary magnetosphere, and leads to a very thin magnetic link between the two bodies. The resulting magnetic configuration of the planet is stable with respect to external perturbations by the stellar wind. Conversely, the open case (lower panels) leads to a much wider magnetic link in the polar region of the planet magnetosphere. The magnetic link in this case is sensitive to external perturbations by the wind. By considering $r_{\rm orb} = 3\,r_\star$, the magnetosphere of the planet is sufficiently close to boundary of the streamer (the open-closed field lines transition region in the stellar wind) that the wind is able to perturb some of the magnetic field lines connecting the two bodies. In the aligned case the magnetic configuration is strong enough to resist this wind perturbation and remain in the closed configuration. On the contrary, the wind is able to drag some of the connecting magnetic field lines in the anti-aligned case, which leads to the observed open configuration. The resulting radially elongated field lines are then forced to episodically reconnect and re-open on the nightside of the planet, as seen in the lower right panel of Figure 5. This phenomenon will provide an additional source of angular momentum loss for the planet. The inclined magnetosphere case (middle panels) lies in between those two configurations. In the cases shown, the planetary field is sufficiently small that its magnetosphere is confined inside the dead-zone and remains in a closed configuration. For more vigorous fields (case D3i2, see Table 3), the inclined magnetosphere also opens into the wind akin to the reversed configuration. Finally, some of the inclined cases regularly flip from a confined to an open configuration. Provided the planetary field is sufficiently small or large, though, one of the two steady configurations is systematically obtained.

The plasma density in the magnetosphere also differs from one case to the other. The magnetospheric plasma has

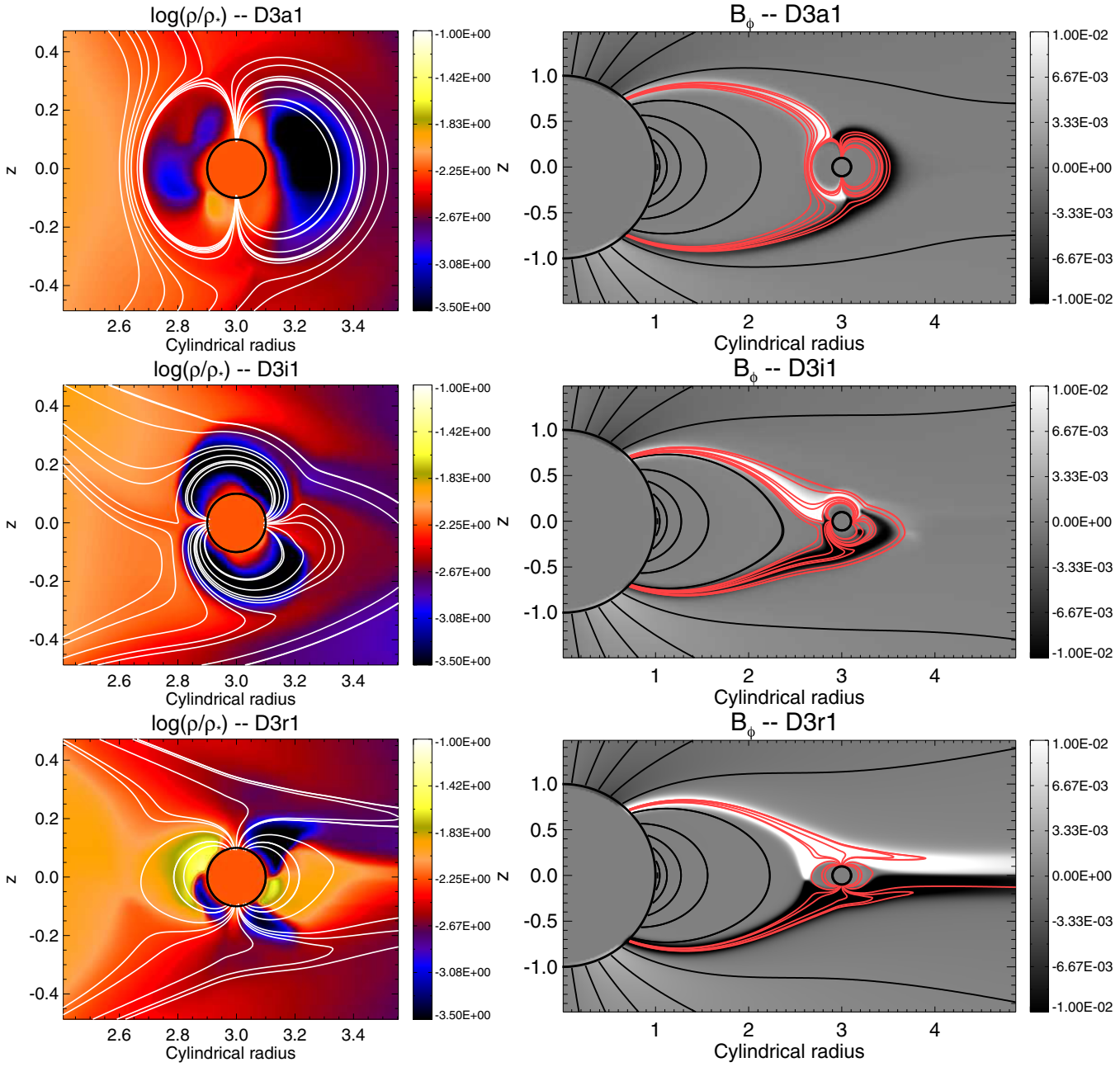

Figure 5. Dipolar interaction solutions for $\theta_0 = 0,\ \pi/2$, and π with $r_{\rm orb} = 3\,r_\star$ (from top to bottom). The quantities shown and layout are the same as in Figure 4. (A color version of this figure is available in the online journal.)

low density in the aligned and inclined cases, with plasma concentrations in the polar regions. The anti-aligned case shows a more complex density structure in the magnetosphere with density concentrations in the magnetic equatorial regions. The depleted regions coincide with the open/closed field line interfaces of the planetary magnetosphere. The detailed density structure here is likely to depend upon the details of the reconnection process in the nightside that is likely affected by the 2.5 reduced by the grid resolution. We observed, by refining the grid, that the overall properties of the star–planet system (such as magnetic torques and angular momentum transfers, see Section 4) were only marginally influenced by the detailed density structure of the planetary magnetosphere. A more accurate modeling of the planetary magnetosphere configuration would require a better control of the reconnection process in the nightside of the magnetosphere.

4. MAGNETIC TORQUES

We now quantify the effects of SPMIs for a range of planetary orbits inside the Alfvén surface, and for both unipolar and dipolar interactions. The Lorentz force associated with the magnetic link between the star and the planet leads to a magnetic angular momentum transfer, as well as a modification of the stellar wind, which we describe in Section 4.1. We characterize the effects of the planetary magnetic field amplitude and inclination (Section 4.2), and the effects of the position of the planet in the wind (Section 4.3) on the torques associated to the SPMI. Finally, we estimate the planet migration induced by the SPMI in Section 4.4.

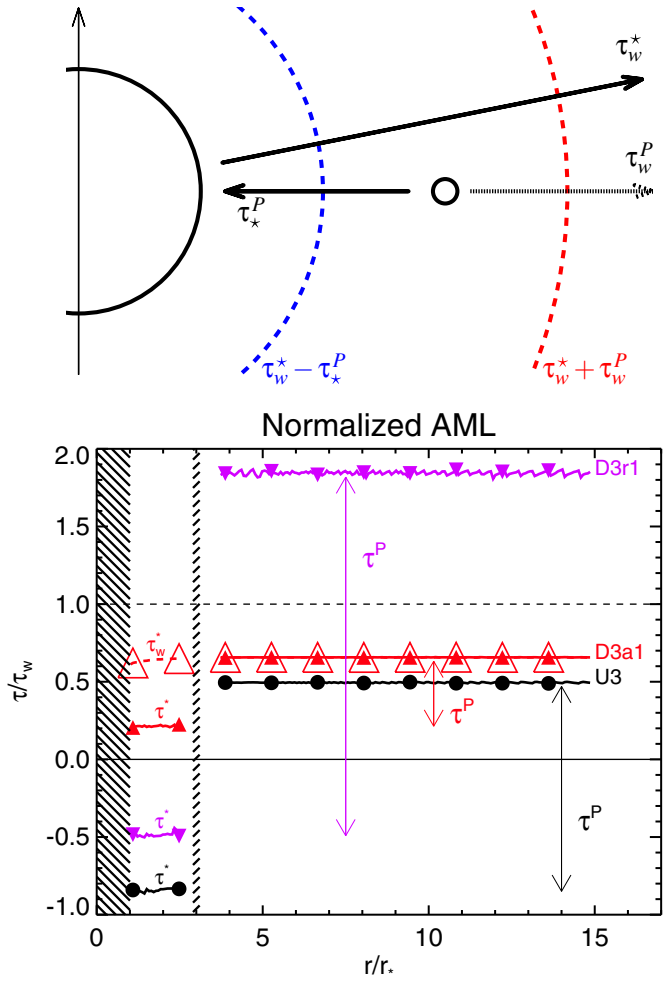

Figure 6. Top: schematic of the angular momentum transfers in a star–planet system. The black arrows show the direction of the angular momentum flux in the cases studied here. They are labeled with the physical sources from which they originate. Bottom: angular momentum loss rate (Equation (7) integrated over spheres) normalized to the fiducial wind AML τ_w, as a function of the spherical radius. The star ($0 \leqslant r \leqslant r_*$) and planet ($r_{\rm orb} = 3\,r_*$) positions are labeled by the hatched zones. Three cases are shown: a unipolar case (U3, black lines), a closed dipolar case (D3a1, red lines) and an open dipolar case (D3r1, magenta lines). The torque applied to the star $\tau^\star$ and applied to the planet τ^P are indicated. The dashed red line shows the outward AML only in case D3a1.

(A color version of this figure is available in the online journal.)

4.1. Angular Momentum Transfers and Stellar Wind Modification

The magnetic connection between the star and the planet leads to a magnetized angular momentum transfer. Since we fix the stellar rotation rate and the orbital motion, the planet and the star act as source and sinks of angular momentum, which is conserved in the stellar wind (Strugarek et al. 2014) and everywhere on our computational grid. As a result, when the system has reached a steady-state, the flux of angular momentum integrated on any spherical surface that is not crossing the stellar or the planetary interior is constant. The top panel of Figure 6 is a schematic of magnetized angular momentum transfers in a star–planet system. The angular momentum flux in between the star and the planet (crossing the dashed blue line) includes both the torque applied by the planet and the torque applied by the wind to the star. It thus corresponds to the overall angular momentum extracted from the star, which we denote $\tau^\star = \tau^\star_P + \tau^\star_w$, with $\tau^\star_P$ the torque applied by the planet to the star and $\tau^\star_w$ the torque applied by the wind to the star. If the star is rotating slowly enough (as it is the case here), the angular momentum is always transferred from the planet to the star and is associated with the torque applied to the planet by the star, which we denote $\tau^P_\star = -\tau^\star_P$. As a consequence, when we compute the AML between the star and the planet, we can account separately for positive and negative contributions and thus properly separate the stellar AML associated with the wind ($\tau^\star_w$) from the one associated with the planet ($\tau^\star_P$). The angular momentum flux outside the orbital radius (crossing the dashed red line) results from the torque applied by the wind to the star ($\tau^\star_w$) and to the planet (τ^P_w). By subtracting the inner and outer AMLs, one readily obtains the torque applied to the planet $\tau^P = \tau^P_\star + \tau^P_w$. The wind contribution to the planetary AML is labeled with dots because in some SPMI cases, the planet does not lose any angular momentum to the wind.

The bottom panel of Figure 6 shows the time-averaged AML (Equation (7) normalized to the fiducial wind AML τ_w) as a function of the spherical radius, for three typical cases (U3, D3a1 and D3r1, see Table 3). As expected, the AML is a piecewise constant function of r, which confirms (1) the conservation of angular momentum and (2) that the models have reached a statistical steady-state.

We immediately remark that the total torque applied to the star (curves lying in $r < 3\,r_\star$) is strongly reduced compared to the fiducial wind torque (black thin line). In some cases, the sign of the net torque on the star is even reversed: the connection between the star and the planet is strong enough such that the net torque is accelerating the star. We recall here that our 2.5D axisymmetric setup overestimates these torques (see discussion in Section 4.3), so the quantitative values of the torques we obtain here need to be checked with 3D simulations.

The red dashed line (with open symbols) shows the $\tau^\star_w$ for the aligned case D3a1. We see that the filtered AML is indistinguishable from the AML calculated for $r > r_{\rm orb}$ which means that—in this particular case—the only torque applied to the planet comes from its magnetic connection to the star. Conversely, we observe that the torque applied to the star–planet system is larger than the fiducial torque in case D3r1, which indicates that the planet is losing angular momentum to both the star and the wind. In order to visualize those direct magnetized transfer of angular momentum, we display the 2.5D angular momentum fluxes in Figure 7 for the fiducial wind and for cases U3 and D3r1. The direction of the angular momentum flux is labeled by the white stream lines and its amplitude by the logarithmic colormap. The angular momentum naturally flows out of the star in the open field line regions (panel (a)) when no planet orbits around the star. In panels (b) and (c), angular momentum directly flows from the planet to the star as well, following the azimuthally elongated "flux-tube" created by the SPMI (see Figures 4 and 5). The wind driving is modified at its foot-point on the stellar surface. The size of the open field line region is accordingly diminished compared to the case of a planet-free wind (panel (a))—which explains the general decrease of the wind torque.

The 2.5D representation of the angular momentum fluxes illustrates the importance of magnetic topology in SPMIs. The unipolar case does not add any fundamental constraint on the stellar wind magnetic topology: the magnetic field lines are simply dragged in the azimuthal direction by the orbiting planet. The anti-aligned case displayed in panel (c) develops the same kind of connection to the star, but the planetary magnetic field

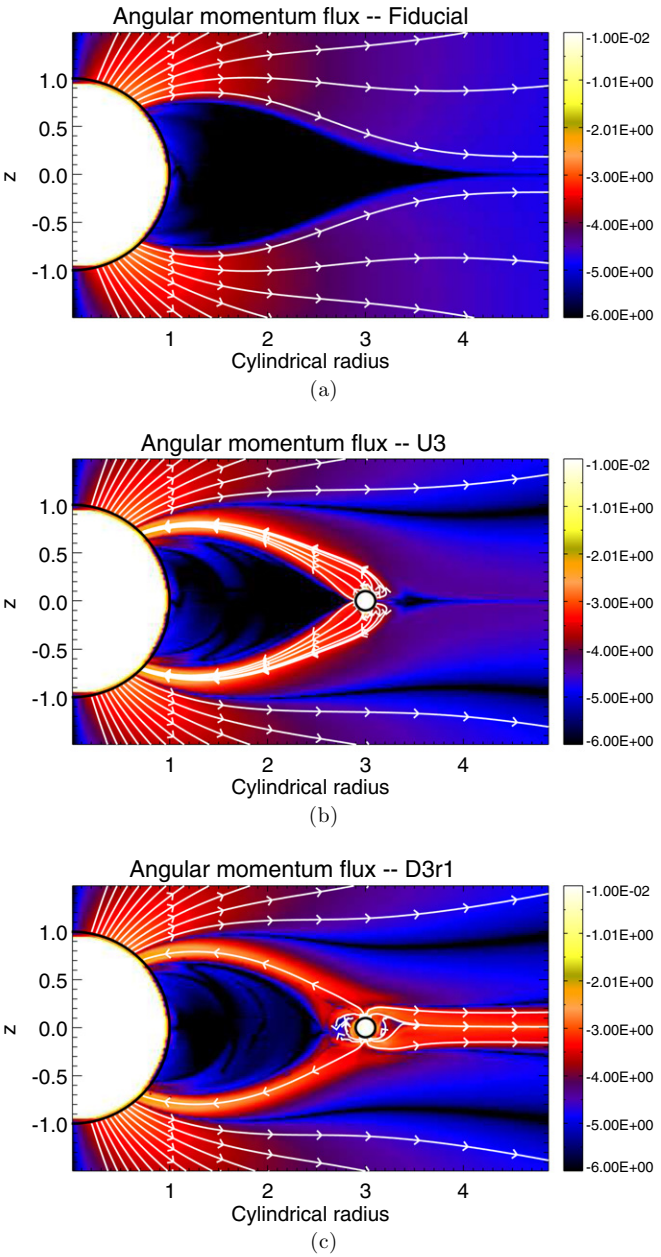

Figure 7. Two-dimensional angular momentum fluxes. The streamlines of angular momentum are labeled by the white lines and arrows, and its amplitude is shown by the background colormap (in logarithmic scale). The planet and stellar surfaces are indicated by the black circles. The cases of (a) the fiducial stellar wind, (b) unipolar, and (c) dipolar ($\theta_0 = \pi$) interactions are shown.

(A color version of this figure is available in the online journal.)

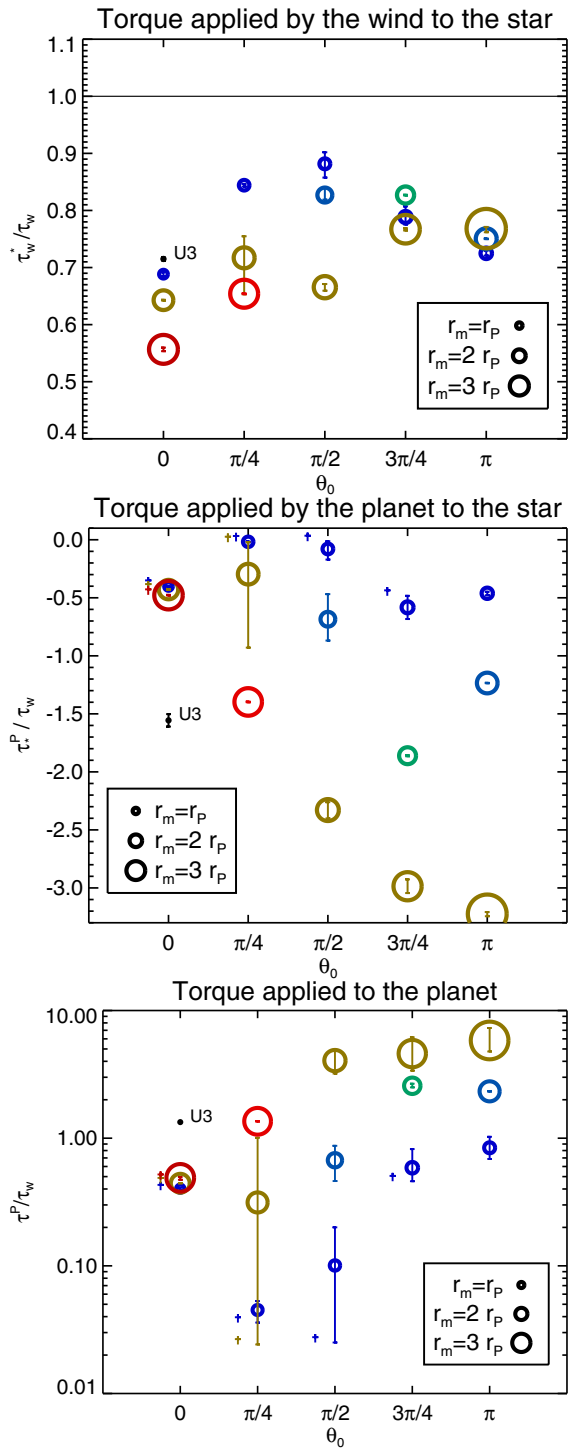

Figure 8. Torques for different planetary field amplitude (colored symbols, from blue–weak to green/yellow–medium to red–strong magnetic fields) and different inclination angles (abscissa). The size of the symbols represent the size of the planetary magnetosphere (see Table 4). We display from top to bottom $\tau_w^\star$, $\tau_P^\star$, and τ^P. In the lower two panels the closed configurations are labeled by †(see the text). The unipolar case U3 is added for reference. Its error bars are obtained for variations over four orders of magnitude of the density level of the planet.

(A color version of this figure is available in the online journal.)

is also able to open up in the accelerating wind region. This interaction is made possible by the closeness of the planet to the dead-zone boundary on the equator and the anti-aligned topology of the planetary magnetic field (see Section 3.3). Hence—as expected from Figure 6—the planet loses angular momentum to both the wind and the star at the same time. We now explore the quantitative sensitivity of the SPMI to the planetary magnetic field strength and topology (Section 4.2), and to the planet position inside the Alfvén surface (Section 4.3).

4.2. Topology and Strength of the Planetary Magnetic Field

The orientation and strength of the planetary magnetic field determines the magnetic coupling efficiency between the two bodies (see Section 3.3). The effect of the magnetic field orientation on its coupling with the coronal field for a close-in planet was initially studied by Ip et al. (2004). In the present work, we include the orbital motion of the planet, which leads to the angular momentum transfer. We display in Figure 8 the

Table 4
Torque Coefficients in the Dipolar Case

τ [τ_w]	c	b	p	t	Θ	s
$\tau_w^\star$ (c)	4.13	492	−0.24	1	0.45 π	2.08
$\tau_P^\star$ (c)	−0.001	1140	0.34	−1	0.37 π	0.77
$\tau_P^\star$ (o)	−0.27	−27.7	0.43	1	0.89 π	1.58
τ^P (c)	0.02	37.0	0.07	−1	0.37 π	0.78
τ^P (o)	0.17	−19.54	0.65	1	0.96 π	1.55

Notes. Closed (c) and open (o) configurations are distinguished. The fit coefficients are defined in Equation (16).

torque applied by the wind (upper panel) and by the planet (middle panel) to the star as a function of the inclination angle θ_0 of the planetary magnetosphere for a planet located at $r_{\rm orb} = 3\,r_\star$. All torques are normalized to the fiducial stellar wind torque. The averaged size of the planetary magnetosphere, measured at the magnetic equator, is given by the size of the circles in the two panels (see Table 3). Their color labels the amplitude of the planetary field, from the smallest (blue, $\mu_P = 4.5 \times 10^{-5}\mu_\star$) to the largest (red, $\mu_P = 4.5 \times 10^{-3}\mu_\star$). The error bars are a measure of the time variations of the torques that occur either because of a flipping between a closed and an open configuration, or because of time-dependent magnetic reconnection on the nightside of the planet. For each inclination angle, the wind modification and $\tau_P^\star$ are directly correlated to the strength of the planetary field (or magnetospheric size). However, the magnetospheric size (or B_P) alone does not appear to be a good proxy to estimate the strength of the SPMI because of the strong dependence on θ_0. The two extreme cases D3a2 and D3r2 reveal the importance of considering the inclination angle of the planetary fields: for comparable magnetospheric dimensions, the torque applied to the planet (bottom panel of Figure 8) varies by an order of magnitude. We generally find that for a given magnetospheric size or for a given μ_p, the torques vary significantly with the inclination angle.

For a given magnetospheric size, the maximum stellar wind modification (upper panel) is obtained for the aligned ($\theta_0 = 0$) configuration. All the aligned cases are in the closed configuration. As a result, for a given magnetospheric size, the magnetic field lines connecting the star to the planet are likely to extend further away from the ecliptic plane and impact higher latitudes—where the wind is driven—at the stellar surface. This is particularly clear in Figure 5 where it can be observed that the connecting field lines impact the stellar surface around $\theta_i \sim 47^\circ$ in the aligned case and around $\theta_i \sim 45^\circ$ in the anti-aligned case. Hence, the maximum wind modification is likely to be obtained in the aligned topology. Conversely, all the anti-aligned cases ($\theta_0 = \pi$) are in the open configuration. As a result, the magnetic link strengthens and is slightly more concentrated as the planetary magnetic field increases. The interacting zone at the stellar surface hence diminishes slightly, and the modification of the stellar wind decreases when the amplitude of the planetary field is increased, leading to an opposite behavior in the completely anti-aligned case, compared to all other inclinations.

The torque applied by the planet to the star (middle panel) and the total torque applied to the planet (lower panel) further reveal different behaviors for the open and closed configurations. In the closed configuration (cases labeled with daggers †), both torques have a surprisingly very weak sensitivity to the amplitude of the planetary field B_P (note that in the inclined cases switching configuration over time, the closed configuration torques are

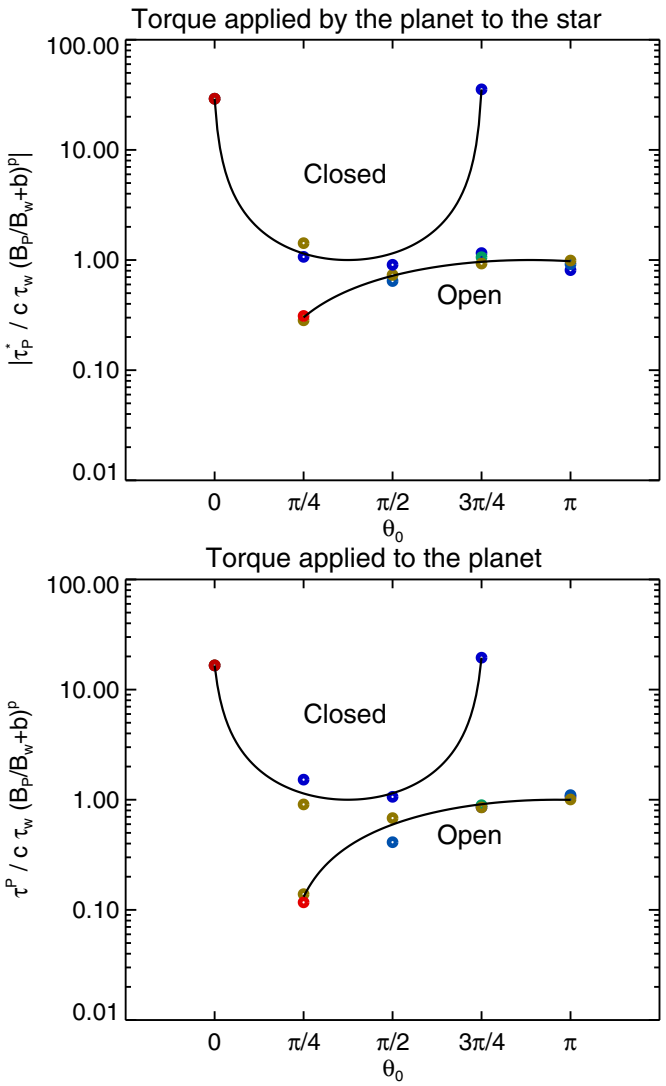

Figure 9. Fit (black lines) of the torque formulation (16) in the dipolar cases. The coefficients of the fits are given in Table 4.
(A color version of this figure is available in the online journal.)

taken at the extremum of the error bars). The torques developing in the open configuration, conversely, depend strongly on both B_P and θ_0. We fit $\tau_P^\star$ and τ^P with the simple formulation

$$\frac{\tau}{\tau_w} = c\left(\frac{B_P}{B_w} + b\right)^p \cos^t\left(\frac{\theta_0 - \Theta}{s}\right) \qquad (16)$$

for each configuration (open "o" and closed "c"). We tested various formulations of the fitting function (16) until an acceptable fit was obtained for the various torques in both the closed and open configurations. The fit coefficients are shown in Table 4 and the fits are visualized in Figure 9 (black lines). The slight discrepancy from the fits is a reasonable trade-off to provide the simple torque formulation (16) for the dipolar interaction. Both torques exhibit the same qualitative behavior.

The magnetic interaction is minimized in the closed configuration for an inclination angle close to $\pi/3$. This results from a simple geometrical constrain in the closed configuration. The field lines connecting the planet to the star—the field lines that are responsible for the transfer of angular momentum—are necessarily anchored at the magnetic poles of the planet. Each planetary pole has to be connected to one—and only one—of

the stellar hemispheres in a stable magnetic configuration (otherwise, strong currents would develop at the planetary poles and the associated magnetic reconnections would tend to suppress such configuration). As a result, in the aligned case the south (resp. north) pole of the planet is connected to the north (resp. south) hemisphere of the star. On one hand, if the planetary dipole is slightly titled, the magnetic connection between the pole the most distant from the star and the stellar hemisphere is harder to establish and the overall magnetic link is weakened. On the other hand, for a perpendicular dipole ($\theta_0 = \pi/2$, middle panel in Figure 5), one of the planetary poles is sufficiently close to the star to reverse this effect. As a consequence, the effective torque is minimized for intermediate inclination angles in the closed configuration. The exact angle is likely to depend on the orbital radius or, said differently, on the relative position of the planet inside the dead-zone. For a planet located at $r_{\rm orb} = 3\,r_\star$ we found that the torque is minimized for $\theta_0 \sim 0.37\pi$.

In the open configuration the torques are maximized for $\theta_0 \sim \pi$. The anti-aligned ($\theta_0 = \pi$) planetary field is naturally compatible with the dipolar structure of the stellar magnetic field, with vertical (along the z direction) field lines near the ecliptic. When the planetary field is inclined from this configuration, the magnetic links at the two poles of the planet are likely to shrink to accommodate the topological constraint. As a result, the connection between the poles of the planet and the stellar hemispheres are weaker and the associated torques decrease, as observed in Figure 9.

4.3. Orbital Radius Dependence

Up to now we have discussed cases with an orbital radius of $3\,r_\star$. We now present cases with variations from $2.5\,r_\star$ to $7\,r_\star$—spanning the whole sub-alfvénic zone—for the unipolar interaction case. We also ran some dipolar cases for particular orbital radii (see Table 3). We display the resulting wind and planetary torques as a function of $r_{\rm orb}$ in Figure 10.

The stellar wind torque is systematically reduced by the orbiting planet (left panel). The decrease is maximized for planets orbiting close to the streamer boundary (the transition region between open and closed field lines of the stellar wind). The magnetic connection has a tendency to inhibit the wind driving at its foot-point on the stellar surface. If the planet orbits too close to the star, the foot-point of the magnetic link on the stellar surface is located well inside the closed field lines region where only a slow (or even no) wind is driven: the SPMI does not significantly modify the stellar wind in this case. If the planet orbits in the open field lines region—and inside the fast Alfvén radius–, the foot-point latitude does not change much with the orbital radius, since the planet remains on the equatorial plane. As a consequence, the strength of the SPMI decreases with the orbital radius due to the combined effects of the decrease of $|v_P - v_\phi|$ ($v_P \propto r_{\rm orb}^{-1/2}$) and the decrease of the stellar wind magnetic field. We match the modification of the stellar wind torque in the unipolar case $\Delta\tau = 1 - \tau_w^\star/\tau_w$ with a Weibull distribution (red line in the left panel of Figure 10) that is given by

$$\Delta\tau = \Delta\tau_0 \left(\frac{r_{\rm orb}}{r_i}\right)^{k-1} e^{-\left(\frac{r_{\rm orb}}{r_i}\right)^k}, \qquad (17)$$

with $(\Delta\tau_0, r_i, k)$ being the free parameters for the fit. We find that the location at which the modification is maximized at the node of the Weibull distribution $r_i((k-1)/k)^{1/k} \sim 3.5\,r_\star = r_a$. The power-law exponent is found to be $k \sim 3.9$.

The torque applied by the planet to the star (right panel with logarithmic axes) also shows two different trends inside and outside the Alfvén radius r_a. For planets orbiting inside r_a, the torque decreases like $r_{\rm orb}^{-4}$. The only other estimation we are aware of was provided by Laine & Lin (2011) in the unipolar case. They found (see their Equation (15), adapted for circular orbits) that the torque scales like $r_{\rm orb}^{-5.5}$. The discrepancy may originate from two effects. First, the 2.5D geometry we consider over-estimates the magnetic torques. One can crudely extrapolate our results by rescaling the torques with a geometrical factor $\alpha_g = r_P/\pi r_{\rm orb}$, which would make the torque decrease like $r_{\rm orb}^{-5}$. The remaining power-law difference with the work of Laine & Lin (2011) could be due to a more subtle geometrical effect. However, it is also likely that it arises from the fact that we consider a magnetic field self-consistently evolving with the dynamical wind, and not constrained to be purely dipolar.

If the planet is orbiting in between the Alfvén and the fast-Alfvén radius, the torque it applies to the star falls off exponentially. The planet in this case is exposed to the accelerating wind, making it hard to establish a magnetic connection with its host. We fit this fall off in the unipolar case with the function (solid blue line in Figure 10)

$$\tau_P^\star = \tau_P^\star(r_a)\, e^{-(r_{\rm orb} - r_a)^{k_f}}, \qquad (18)$$

with $k_f = 2.3$. Note that the exact exponential fall-off may differ between the dipolar and unipolar cases. For reference we plotted the same curve for $k_f = 2$ (dashed blue line) and $k_f = 3$ (dotted blue line).

The dipolar cases (orange and green triangles in the two panels of Figure 10) show a significant spread across the scaling law we derived from the unipolar cases. By using Equation (16) to get rid of the (B_P, θ_0) dependence in the closed and open configurations, this spread is significantly reduced (not shown here). The dipolar cases are then observed to follow the same trends with the orbital radius, albeit with different proportionality factors that could be properly determined with a larger set of dipolar models at different orbital radii.

It was previously argued that an SPMI involving a close-in planet would generally decrease the stellar wind angular momentum loss because the planet would block a significant part of the outgoing stellar wind (Cohen et al. 2010). Here we also find—provided the star rotates sufficiently slowly, see Figure 3—that SPMI generally reduces the magnetic torque applied to the central star. We find that the net torque applied to the star is decreased primarily because of the direct transfer of angular momentum from the planet to the star. The SPMI also leads to a modification of the wind driving at the stellar surface, which in turns leads to a reduction of the torque applied by the wind to the star. This effect, which we believe to be at the origin of the "blocking" effect identified by (Cohen et al. 2010), is found to be generally less important. Our results nevertheless also support the idea that SPMI could partly explain the empirical evidence of excess of rotation observed in stars hosting close-in planets (see also Pont 2009).

4.4. Planet Migration

The magnetic link that connects the planet and the star together leads to a torque that applies to the two celestial bodies. The resulting angular momentum transfer changes the stellar rotation and the planetary orbit. The spin-angular momentum J

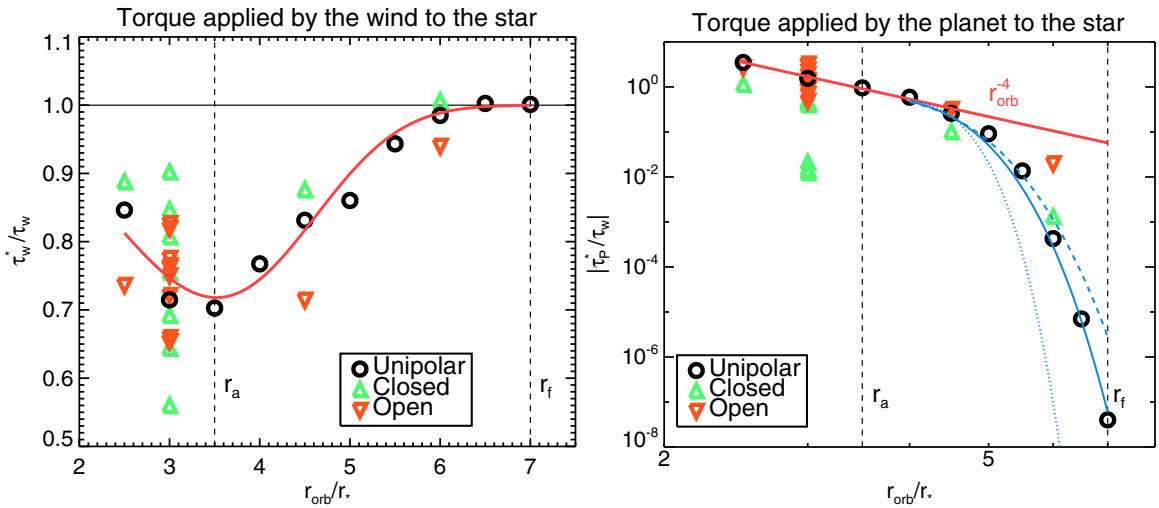

Figure 10. Normalized magnetic torques as a function of the orbital radius. Black circles label the unipolar cases, and the upward and downward triangles label the dipolar cases in the closed and open configurations. The left panel shows the torque applied by the stellar wind. The modification of the stellar wind torque is fitted with a Weibull distribution (red curve, see the text). The right panel shows the torque applied by the planet to the star with logarithmic scales. The cases with a planet inside the Alfvén radius r_a are well matched by a $r_{\rm orb}^{-4}$ power law. In the two panels the position of the Alfv´en r_a and fast Alvén r_f surfaces on the equator are shown by the vertical dashed lines.

(A color version of this figure is available in the online journal.)

of the host star and the orbital angular momentum of the planet can be defined by

$$J_\star = I_\star \Omega_\star \sim k^2 M_\star r_\star^2 \Omega_\star \,, \tag{19}$$

$$J_P = I_P \omega_{\rm orb} = M_P r_{\rm orb}^2 \omega_{\rm orb} \,, \tag{20}$$

where I represents the moment of inertia and $\omega_{\rm orb} = \sqrt{GM_\star / r_{\rm orb}^3}$. The normalized radius of gyration k^2 is of order 0.1 for a main sequence solar-like star. $I_\star$ is generally slightly higher than I_P for close-in planets. The angular momentum ratio is given by

$$\frac{J_P}{J_\star} = \frac{M_P}{k^2 M_\star} \left(\frac{r_{\rm orb}}{r_\star} \right)^{1/2} f^{-1} \,. \tag{21}$$

The full range of our models is between $J_P/J_\star \sim 40$ (for $r_{\rm orb} = 3\,r_\star$) and 60 (for $r_{\rm orb} = 7\,r_\star$), which shows that, in all cases, the orbital angular momentum of the planet is higher than the rotational angular momentum of the star. This dominance is due to the relatively slow rotation of the star (the planet, in this work, is always inside the co-rotation radius, see Figure 3).

Whether or not the effect of SPMI is significant depends on the timescale over which angular momentum is transferred between the two bodies. Based on the angular momentum definitions (20), we define the evolution timescale

$$t_P = \frac{r_{\rm orb}}{\dot{r}_{\rm orb}} = 2 \frac{J_P}{|\tau^P|} \,, \tag{22}$$

where the factor 2 comes from the $r_{\rm orb}^{1/2}$ dependence of J_P. We plot the migration timescales assuming the case of a large stellar magnetic field, $B_\star = 246$ G in Figure 11. In the unipolar case and dipolar cases in the closed configuration, the amplitude of the torque applied to the star by the planet and of the net torque applied to the planet are very similar, since the planet loses a negligible amount of angular momentum to the wind. Based on the scaling found in Section 4.3, we expect the migration time

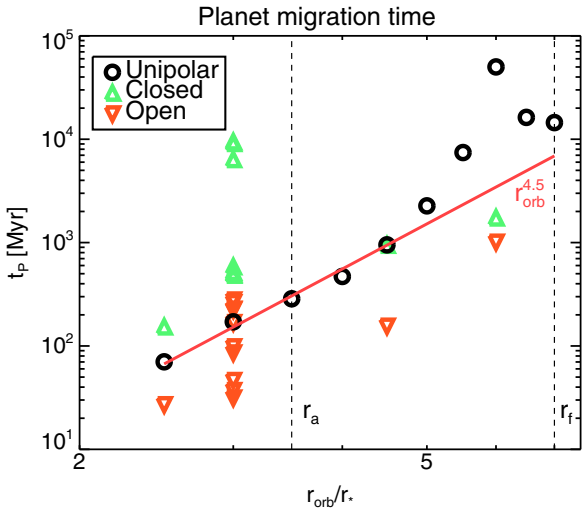

Figure 11. Migration timescale as a function of the orbital radius for $B_\star = 246$ G. The migration timescale is fitted by a power-law, shown in red (see the text for details).

(A color version of this figure is available in the online journal.)

to scale with $r_{\rm orb}^{4.5}$ (see Equation (22)). We overplot this scaling in red in Figure 11 and indeed observe a general agreement for the innermost planets.

The migration time in the unipolar case then increases exponentially in between the Alfvén surfaces, but appears to go back to a constant value near the fast Alfvén surface boundary. In this region the planet is subject to a direct interaction with the fast stellar wind and hence starts—in the unipolar case—to lose angular momentum to the wind only. The dead-zone rotates at the stellar rotation rate whereas the open field line region trails behind at a lower rotation rate. When the planet is completely outside the dead-zone, it interacts with a more slowly rotating plasma which enhances the differential motion driving the SPMI. As a result, we observe a discontinuity in the migration timescale of the planet. It is worth noting that, even if the planet

were outside the fast Alfvén radius, it would still undergo an orbital decay linked to its interactions with the rotating wind. It would eventually enter the dead-zone and magnetically interact with its host, if the system lives long enough. We ran a couple of other models (not shown here) with orbital radii between 7 and $10\,r_\star$ showing that the decay timescale remains approximately constant within a few stellar radii outside the Alfvén surface.

The migration timescales in the dipolar cases span two orders of magnitude, depending on the amplitude and inclination of the planetary magnetic field. We note again that the topology of the planetary field has a dramatic influence on the SPMI: a planet in the open configuration will systematically lose orbital angular momentum much faster than a planet in the closed configuration. For more realistic stellar magnetic configurations, the topology is likely to switch back and forth aligned and anti-aligned configurations as the planet orbits inside the complex coronal magnetic field. Our results show that the time-averaged torque applied to the planet would be largely dominated by anti-aligned phases. Hence, such configuration should be used when estimating migration timescales due to SPMIs in real star–planet systems. The dipolar cases in the open configuration seem to roughly follow the same power-law as the unipolar and closed cases, for fixed values of inclination and strength of the planetary field (not shown here). However, the grid of models presented here does not allow us to properly verify the power-law exponent in the open configuration, which would require additional simulations at several orbital radii. In addition, it must be stated that a planetary outflow (powered by, e.g., stellar radiation) could also modify this power-law.

The planet migration timescales with $B_\star^2$. If one considers a star with a lower magnetic field (e.g., $B_\star = 0.78$ G), the migration timescales shown in Figure 11 are five orders of magnitude larger, and the SPMI clearly does not play a significant role in the planet migration during the whole system life-time. On the other hand, for the larger stellar magnetic field shown ($B_\star = 246$ G), the planet migrates inside the dead-zone on a timescale ranging from approximately 20 to 20,000 Myr. Thus, in some cases the timescales can be much shorter than the secular evolution of the system: in these cases SPMI is certainly one of the major effects on the planetary orbit.

5. TOWARD GENERAL FORMULATIONS OF THE TORQUES

In order to compile all the SPMI effects together for the unipolar and dipolar interactions, we propose hereafter a formulation for the torques applied to the star and the planet. We also apply the geometrical factor α_g to account for the reduced 2.5D geometry used in this work.

The final torque that applies to the star results from the modified stellar wind and from the torque applied to the planet. It can be written in the following form.

$$\tau^\star = \tau_w \{Q_\Upsilon + Q_P\} , \tag{23}$$

where τ_w is the fiducial wind torque which can be obtained from Matt et al. (2012); Réville et al. (2014), Q_Υ is the ratio quantifying the modification of the open flux due to the SPMI, and Q_p is the normalized torque associated with the orbiting planet. From Section 4 we can write

$$Q_\Upsilon = 1 - \alpha_g \Delta\tau , \tag{24}$$

with $\Delta\tau$ given by Equation (17). Q_P is given by

$$Q_P = \left(\frac{r_{\rm orb}}{r_\star}\right)^{-5} \mathcal{H}_P , \tag{25}$$

where $\mathcal{H}$ is defined in the unipolar and dipolar cases by

$$\mathcal{H}_P^u = C_0 \tag{26}$$

$$\mathcal{H}_P^d = C_1 \left(\frac{B_P}{B_w} + b\right)^p \cos^t\left(\frac{\theta_0 - \Theta}{s}\right) . \tag{27}$$

The parameters defining $\mathcal{H}_P^d$ can be found in Table 4 for both the open and closed configurations.

The total magnetic torque that applies to the orbiting planet includes the torque from the star and the one from the wind. We combine the results from Sections 4.2 and 4.3 to obtain the following torque formulation

$$\tau^P = \tau_w C_2 \left(\frac{r_{\rm orb}}{r_\star}\right)^{-5} \left(\frac{B_P}{B_w} + b\right)^p \cos^t\left(\frac{\theta_0 - \Theta}{s}\right) \tag{28}$$

where the parameters $(b,\ p, t, \Theta, s)$ depend on the configuration and are given in Table 4.

The exact multiplicative constants (C_0, C_1 and C_2) are likely to depend on the radius of the planet, which we did not vary in this study. C_0 also depends on the grid resolution and should also be calibrated with simulations done in 3D geometry. Hence, the numerical value of those multiplicative constants needs to be considered with caution.

6. CONCLUSIONS

In this work we have explored the efficiency of the magnetic interactions between a star and a close-in planet to transfer angular momentum. We explored the differences between the cases of a magnetized (dipolar interaction) and non-magnetized (unipolar interaction) planets. Our results can be summarized as follows.

1. The SPMI systematically decreases the torque applied by the stellar wind. This effect is maximized when the planet is in orbit close to streamer boundaries (the open/closed field line transition region) in the corona.
2. When the star rotates slowly (as considered here), the torque applied by the planet to the star is generally higher than the decrease of the torque applied by the wind. It can even compete with the total angular momentum removed by the wind, and in some cases result in a net increase of angular momentum for the star.
3. The torque applied by the planet to its host star is qualitatively similar in the unipolar and in the dipolar cases, but differs significantly in its amplitude.
4. Two magnetic configurations can be encountered in the dipolar case, where the planetary magnetosphere is either confined around the planet (the so-called closed configuration) or where it opens in the stellar wind (the so-called open configuration).
5. In the dipolar case, the angle of inclination of the planetary field with respect to the coronal field can greatly modify the efficiency of the SPMI. The knowledge of both the magnetospheric size and the inclination angle of the planetary field is needed to estimate the angular momentum transfers between the star and the planet.

6. The planet migration associated to the SPMI is unstable inside the Alfvén surface. A planet in orbit inside (resp. outside) the co-rotation radius will systematically migrate inward (resp. outward). Furthermore, the magnetic interaction with a planet inside the Alfvén surface strengthens with time and leads to an accelerated decay of the orbiting planet. This effect may be counterbalanced only if other processes (e.g., tidal forces in multi-planet systems) are taken into account. Provided the star is rotating sufficiently fast, a stable point for the SPMI can also exist outside the Alfvén surface where the planet is in co-rotation with the rotating wind.
7. The migration timescale linked to the SPMI is shown to be sufficiently short in some cases (particularly when the magnetic fields are strong), demonstrating the SPMI to be a first order effect in the secular evolution of the star–planet system (see Section 4.4).
8. The torque applied to the planet, in the dipolar interaction case, is strongest in the open configuration. Therefore, the open configuration state is likely to dominate long-term transfers of angular momentum and should be preferred to estimate the potential contribution of the SPMI to the planetary migration.
9. Empirical scaling laws for the wind modification, the torque between the star and the planet, and the planet migration time were proposed and summarized in Section 5.

To further refine the scaling laws we derived, several improvements are needed. The first obvious limitation of this work lies in its reduced geometry. Fully 3D simulations will be needed to adequately validate the scaling laws (Section 5), and especially the multiplicative constants in front them (Equations (17) and (26)–(28)). They would also allow us to take into account the eventual rotation of the planet for non-synchronized star–planet systems. All the types of unipolar interactions that we did not considered here (see Section 3.2) could also be explored with 3D simulations.

Second, real stars possess much more complex magnetic structures in their corona. Even though our formulae give first order estimates of the torques acting in the system, they were derived with a dipolar topology of the stellar magnetic field, for which the dead-zone is on the ecliptic. This is not the case for, e.g., a quadrupolar-dominated wind (see, e.g., Pinto et al. 2011, for wind simulations with various realistic magnetic topologies). In addition, real stellar magnetic field are generally non-axisymmetric. Hence, calculating the torque in the general case would require 3D simulations, to take into account their temporal and spatial variation in the stellar corona obtained either from numerical simulations (Brun et al. 2004; Ghizaru et al. 2010; Brown et al. 2010; Käpylä et al. 2012) or observations (see, e.g., Petit et al. 2008; Fares et al. 2013).

Third, we explored the SPMIs for a planet with a fixed radius and a fixed mass. The dependence of the scaling laws we proposed should also be characterized with respect to those planetary parameters.

Finally, we focused this first study on magnetic interactions. It is certainly possible to retain more physical effects in our model. Radiative transfer should be taken into account, to be able to model the "induced magnetosphere" unipolar case (Venus-like) and planetary outflows (Trammell et al. 2014). Tidal interactions provide another major mechanism for angular momentum transfer and should be treated self-consistently with the SPMI, in order to develop a unified theory of angular momentum transfers in star–planet systems. The model we presented in this work can be used as a basis for a global modeling framework of star–planet systems.

We thank the anonymous referee for valuable comments on our manuscript. A.S. thanks A. Cumming, R. Pinto, A. Vidotto, and P. Zarka for discussions about stellar winds and star–planet interactions. This work was supported by the ANR 2011 Blanc Toupies and the ERC project STARS2. A.S. acknowledges support from the Canada's Natural Sciences and Engineering Research Council. We acknowledge access to supercomputers through GENCI (project 1623), Prace, and ComputeCanada infrastructures.

REFERENCES

Abreu, J. A., Beer, J., Ferriz-Mas, A., McCracken, K. G., & Steinhilber, F. 2012, A&A, 548, 88
Auclair-Desrotour, P., Le Poncin-Lafitte, C., & Mathis, S. 2014, A&A, 561, L7
Barker, A. J., & Ogilvie, G. I. 2011, MNRAS, 417, 745
Bolmont, E., Raymond, S. N., Leconte, J., & Matt, S. P. 2012, A&A, 544, 124
Brown, B. P., Browning, M. K., Brun, A. S., Miesch, M. S., & Toomre, J. 2010, ApJ, 711, 424
Brun, A. S., Browning, M. K., Dikpati, M., Hotta, H., & Strugarek, A. 2013, SSRv, 1
Brun, A. S., Miesch, M. S., & Toomre, J. 2004, ApJ, 614, 1073
Charbonneau, P. 2010, LRSP, 7, 3
Charbonneau, P. 2013, Natur, 493, 613
Cohen, O., Drake, J. J., Glocer, A., et al. 2014, ApJ, 790, 57
Cohen, O., Drake, J. J., Kashyap, V. L., Sokolov, I. V., & Gombosi, T. I. 2010, ApJL, 723, L64
Cohen, O., Kashyap, V. L., Drake, J. J., et al. 2011, ApJ, 733, 67
Cuntz, M., Saar, S. H., & Musielak, Z. E. 2000, ApJL, 533, L151
Donati, J.-F., Moutou, C., Fares, R., et al. 2008, MNRAS, 385, 1179
Evans, C. R., & Hawley, J. F. 1988, ApJ, 332, 659
Fares, R., Donati, J.-F., Moutou, C., et al. 2010, MNRAS, 406, 409
Fares, R., Moutou, C., Donati, J.-F., et al. 2013, MNRAS, 435, 1451
Gardiner, T. A., & Stone, J. M. 2005, JCoPh, 205, 509
Ghizaru, M., Charbonneau, P., & Smolarkiewicz, P. 2010, ApJL, 715, L133
Goldreich, P., & Lynden-Bell, D. 1969, ApJ, 156, 59
Hellier, C., Anderson, D. R., Collier Cameron, A., et al. 2009, Natur, 460, 1098
Ip, W.-H., Kopp, A., & Hu, J.-H. 2004, ApJL, 602, L53
Jardine, M., & Collier Cameron, A. 2008, A&A, 490, 843
Jones, C. A. 2011, AnRFM, 43, 583
Käpylä, P. J., Mantere, M. J., & Brandenburg, A. 2012, ApJL, 755, L22
Kashyap, V. L., Drake, J. J., & Saar, S. H. 2008, ApJ, 687, 1339
Keppens, R., & Goedbloed, J. P. 1999, A&A, 343, 251
Keppens, R., & Goedbloed, J. P. 2000, ApJ, 530, 1036
Kivelson, M. G., Bagenal, F., Kurth, W. S., et al. 2004, in Jupiter. The planet, Satellites and Magnetosphere, ed. F. Bagenal, T. E. Dowling, & W. B. McKinnon (Cambridge: Cambridge Univ. Press), 513
Kivelson, M. G., & Ridley, A. J. 2008, JGR, 113, 5214
Lai, D., Helling, C., & van den Heuvel, E. P. J. 2010, ApJ, 721, 923
Laine, R. O., & Lin, D. N. C. 2011, ApJ, 745, 2
Laine, R. O., Lin, D. N. C., & Dong, S. 2008, ApJ, 685, 521
Lammer, H., Bredehöft, J. H., Coustenis, A., et al. 2009, A&ARv, 17, 181
Lanza, A. F. 2008, A&A, 487, 1163
Lanza, A. F. 2009, A&A, 505, 339
Lanza, A. F. 2010, A&A, 512, 77
Lanza, A. F. 2012, A&A, 544, 23
Lecavelier des Etangs, A., Ehrenreich, D., Vidal-Madjar, A., et al. 2010, A&A, 514, 72
Lovelace, R. V. E., Mehanian, C., Mobarry, C. M., & Sulkanen, M. E. 1986, ApJS, 62, 1
Lovelace, R. V. E., Romanova, M. M., & Barnard, A. W. 2008, MNRAS, 389, 1233
Ma, Y. J., Nagy, A. F., Russell, C. T., et al. 2013, JGR, 118, 321
Mathis, S., Alvan, L., & Remus, F. 2013, in Role and Mechanisms of Angular Momentum Transport During the Formation and Early Evolution of Stars Evry Schatzman School 2012, ed. P. Hennebelle & C. Charbonnel (EAS Publications Series, Vol. 62; Cambridge: Cambridge Univ. Press), 323
Matt, S., & Balick, B. 2004, ApJ, 615, 921
Matt, S., & Pudritz, R. E. 2005, MNRAS, 356, 167
Matt, S., & Pudritz, R. E. 2008, ApJ, 678, 1109

Matt, S. P., MacGregor, K. B., Pinsonneault, M. H., & Greene, T. P. 2012, ApJL, 754, L26
Mestel, L. 1968, MNRAS, 138, 359
Mignone, A., Bodo, G., Massaglia, S., et al. 2007, ApJS, 170, 228
Miller, B. P., Gallo, E., Wright, J. T., & Dupree, A. K. 2012, ApJ, 754, 137
Neubauer, F. M. 1980, JGR, 85, 1171
Neubauer, F. M. 1998, JGR, 103, 19843
Parker, E. N. 1958, ApJ, 128, 664
Parviainen, H., Gandolfi, D., Deleuil, M., et al. 2014, A&A, 562, 140
Petit, P., Dintrans, B., Solanki, S. K., et al. 2008, MNRAS, 388, 80
Pinto, R. F., Brun, A. S., Jouve, L., & Grappin, R. 2011, ApJ, 737, 72
Pont, F. 2009, MNRAS, 396, 1789
Poppenhaeger, K., & Wolk, S. J. 2014, A&A, 565, L1
Réville, V., Brun, A. S., Matt, S. P., & Strugarek, A. 2014, ApJ, submitted
Rubenstein, E. P., & Schaefer, B. E. 2000, ApJ, 529, 1031
Russell, C. T. 1993, RPPh, 56, 687
Scharf, C. A. 2010, ApJ, 722, 1547
Selsis, F., Kasting, J. F., Levrard, B., et al. 2007, A&A, 476, 1373
Shibata, K., Isobe, H., Hillier, A., et al. 2013, PASJ, 65, 49
Shibayama, T., Maehara, H., Notsu, S., et al. 2013, ApJS, 209, 5
Shkolnik, E., Bohlender, D. A., Walker, G. A. H., & Collier Cameron, A. 2008, ApJ, 676, 628
Shkolnik, E. L. 2013, ApJ, 766, 9
Shkolnik, E. L., Walker, G. A. H., Bohlender, D. A., Gu, P. G., & Kürster, M. 2005, ApJ, 622, 1075
Southworth, J., Hinse, T. C., Dominik, M., et al. 2009, ApJ, 707, 167
Stevenson, D. J. 2003, E&PSL, 208, 1
Strugarek, A., Brun, A. S., & Matt, S. 2012, in Proc. of the Annual Meeting of the French Society of Astronomy and Astrophysics, ed. S. Boissier (SF2A), 419
Strugarek, A., Brun, A. S., Matt, S. P., & Réville, V. 2014, in IAU Symp. 300, Nature of Prominences and Their Role in Space Weather, ed. B. Schmieder, J.-M. Malherbe, & S. T. Wu (Cambridge: Cambridge Univ. Press), 330
Trammell, G. B., Li, Z.-Y., & Arras, P. 2014, ApJ, 788, 161
ud Doula, A., & Owocki, S. P. 2002, ApJ, 576, 413
Vidotto, A. A., Fares, R., Jardine, M., et al. 2012, MNRAS, 423, 3285
Vidotto, A. A., Jardine, M., Morin, J., et al. 2014, MNRAS, 438, 1162
Vidotto, A. A., Opher, M., Jatenco-Pereira, V., & Gombosi, T. I. 2010, ApJ, 720, 1262
Washimi, H., & Shibata, S. 1993, MNRAS, 262, 936
Zanni, C., & Ferreira, J. 2009, A&A, 508, 1117
Zarka, P. 2007, P&SS, 55, 598
Zhang, M., & Penev, K. 2014, ApJ, 787, 131